Dipolar magnetic fields of spin excitations in vortex-state cylindrical ferromagnetic dots

R. Zivieri[1,2] and F. Nizzoli[2,1]
[1]*CNISM Unità di Ricerca di Ferrara, Via Saragat 1, I-44100 Ferrara, Italy*
[2]*Dipartimento di Fisica, Università di Ferrara, Via Saragat 1, I-44100 Ferrara, Italy*
(Received 19 December 2007; revised manuscript received 24 April 2008; published 18 August 2008)

A study of the effects of the dynamic dipolar magnetic fields on spin mode dynamics in circular cylindrical magnetic dots in vortex-state at zero applied fields is presented. The out-of-core and core dipolar magnetic fields are calculated exactly for both axially symmetric and nonaxially symmetric spin modes in terms of the nonlocal tensorial Green's-function. The exactly calculated spin mode eigenfrequencies are compared with those obtained using the local dipolar approximation for permalloy disks. The validity of the local dipolar approximation is discussed for radii ranging from the nanometric to the micrometric scale and for different thicknesses in the nanometric range. In the comparison both the case where the dynamic magnetization is assumed uniform along the thickness and the case where a thickness dependence is present are considered. In this framework, a simple formula giving the frequency splitting of the nonaxially symmetric modes $(\pm|m|,n)$ is obtained. The calculated splitting compares well with the measured splitting at different aspect ratios. We also show that the general effect of the static exchange field arising from the "curling" configuration causes a downshift of the spin mode frequencies in nanometric dots. This behavior is similar to that of the demagnetizing field in the saturated state.

DOI: 10.1103/PhysRevB.78.064418 PACS number(s): 75.75.+a, 75.30.Ds

I. INTRODUCTION

In the last years a great deal of studies and a large extent of experimental work have been performed to study the static and the dynamical properties of ferromagnetic particles of different shape and size in the "curling" configuration.[1–7] This work is also due to the improvements in the fabrication and sample preparation techniques. In particular, planar magnetic dots have been widely investigated and have shown a magnetic behavior different from the one of the continuous films because of the lateral confinement.[8]

A significant difficulty in the calculations is due to the nonlocal nature of the magnetostatic interaction, because in order to study the dynamical properties of a curling configuration one should solve an integral-differential equation. Recent numerical methods based on micromagnetic approaches have been successful in the calculation of the dipolar terms.[8–10] A great advantage of these methods is represented by the fact that confined magnetic elements of different shapes and in different ground states may be studied. However, the micromagnetic approaches often suffer from the limitation in the system dimensions that were studied, which are more difficult to treat when the system is in the micrometric range.

Conversely, analytical approaches developed very recently have solved the problem of evaluating the dipole-dipole interactions in the vortex state at zero applied field considering thin cylindrical dots and thus neglecting the effect of tridimensionality.[2,3,7,11,12] In our previous study, in order to partially overcome the difficulty of calculating the dipole-dipole interaction,[13] the tridimensionality effect was studied within the local dipolar approximation also in dots of moderate aspect ratio. The main aim of this study is, thus, the exact calculation of the dipole-dipole interaction of both axially symmetric and nonaxially symmetric normal modes in cylindrical ferromagnetic dots from nanometric to micrometric size. The calculation is done in the vortex state at zero applied fields taking into account the effect of tridimensionality. In this way, we also give an estimation of the effect of magnetization nonuniformity along the thickness on the mode frequencies. Furthermore, we discuss the mode frequency deviation from the linear dependence from $\sqrt{L/R}$ found in dots of moderate aspect ratio, where L is the dot thickness and R is the dot radius. Instead, it is well known[3,4,7,11,12] that the linear dependence of the frequency from $\sqrt{L/R}$ is the typical behavior of spin excitations in the ultrathin dot limit. We do not take into account the interdot magnetostatic energy, supposing in the calculations the arrays of dots at a distance equal or larger than the dot diameter. Since we deal with permalloy (Py) dots where anisotropy effects are (in general) small, we also neglect any anisotropy contribution. Moreover, we are also able to give a quantitative derivation of the frequency splitting of the nonaxially symmetric modes obtaining a very good agreement of the calculated $m=\pm 1$ frequency splitting with available measurements.[5,7,8,14] The analytical models developed up to now[1,7,12,13] have underestimated it, while micromagnetic simulations often tend to overestimate the experimental data (see, e.g., Ref. 6).

II. EQUATIONS OF MOTION AND TORQUE MOMENTS

The total magnetization is expressed as the sum of a static and a small dynamic part, viz. $\mathbf{M}(\mathbf{r},t)=\mathbf{M}_0+\mathbf{m}(\mathbf{r},t)$ with the small dynamic part that can be written as $\mathbf{m}(\mathbf{r},t)=\mathbf{m}_0 r(\rho)e^{im\phi}e^{ik_{\perp}z}e^{-i\omega t}$ choosing a cylindrical (ρ,ϕ,z) reference frame; $\mathbf{m}_0$ is the dynamic magnetization amplitude proportional to the saturation magnetization M_s, $r(\rho)$ is a radial function, and ω is the spin mode frequency. The ground-state static magnetization in the out-of-core (OC) region takes the form $\mathbf{M}_0=(0,M_{\phi}^{\mathrm{OC}},0)$, with $|\mathbf{M}_0|=M_s$ and its deviation from equilibrium may be written as $\mathbf{m}_{\mathrm{OC}}=(m_{\rho},0,m_z)$. Indeed, the

deviation from the ground state of the azimuthal component of $\mathbf{m}$ along the unit vector, $\hat{\phi}$ and m_ϕ, is much smaller[10] with respect to m_ρ and m_z. The amplitudes $m_{o\rho}$ and m_{0z} are complex. Moreover, in the OC region $|M_z| \ll |M_\phi^{\mathrm{OC}}|$ so that $|M_\phi^{\mathrm{OC}}| \simeq M_s$. In the core (C) region, the ground-state static magnetization is $\mathbf{M}_0=(0,M_\phi^{\mathrm{C}},M_z)$, with $M_\phi^{\mathrm{C}}=M'_{\phi'}$ sin θ and $M_z=M'_{\phi'}$ cos θ obtained by means of $R^{-1}(\psi)=R(-\psi)$. $R(\psi)$ is the rotation matrix defined by the Euler angles $(0,\psi,0)$ with respect to two Cartesian frames, one fixed (x,y,z) and the other, (x',y',z'), rotated by $\psi=\pi/2-\theta$ about the x axis with $x=x'$ and θ is the polar angle (Ref. 13). $M'_{\phi'}$ corresponds thus to the M_ϕ^{OC} component in the fixed reference frame so that $M'_{\phi'}$ may be substituted by M_ϕ^{OC}.

Due to the rotation of the precession plane in the C region $(0 \le \rho \le a)$ with a, the C radius a m_ϕ^{C} component arises so that the dynamic magnetization may be expressed as $\mathbf{m}_{\mathrm{C}}=(m_\rho,m_\phi^{\mathrm{C}},m_z^{\mathrm{C}})$ with $m_\phi^{\mathrm{C}}(\mathbf{r},t)=-m'_{z'}(\mathbf{r},t)\cos\theta$ and $m_z^{\mathrm{C}}(\mathbf{r},t)=m'_{z'}(\mathbf{r},t)\sin\theta$. The component $m'_{z'}$ is the z component of the dynamic magnetization with respect to the local rotated reference frame (x',y',z') in the C region and corresponds to the m_z component of the fixed (x,y,z) reference frame so that $m'_{z'}$ may be substituted by m_z. The m_ϕ^{C} and m_z^{C} components are obtained by means of $R(-\psi)$ applied to $m'_{z'}$.

Omitting the space and time dependences, we write down the linearized equation of motion obtained neglecting the second-order dynamic terms[13]

$$-\frac{1}{\gamma}\frac{\partial \mathbf{m}}{\partial t}=\mathbf{m}_{\mathrm{OC}}\times\mathbf{H}_{\mathrm{eff}}^{\mathrm{OC}}+\mathbf{M}_0\times\mathbf{h}_{\mathrm{eff}}^{\mathrm{OC}}+\mathbf{m}_{\mathrm{C}}\times\mathbf{H}_{\mathrm{eff}}^{\mathrm{C}}+\mathbf{M}_0\times\mathbf{h}_{\mathrm{eff}}^{\mathrm{C}}, \tag{1}$$

where $\gamma>0$ is the gyromagnetic ratio. As we are not interested in time decaying of spin modes, we neglect the damping term. The static effective field $\mathbf{H}_{\mathrm{eff}}=\mathbf{H}_{\mathrm{eff}}^{\mathrm{OC}}+\mathbf{H}_{\mathrm{eff}}^{\mathrm{C}}$ is expressed by means of its OC and C static fields, $\mathbf{H}_{\mathrm{eff}}^{\mathrm{OC}}$ and $\mathbf{H}_{\mathrm{eff}}^{\mathrm{C}}$, respectively; $\mathbf{h}_{\mathrm{eff}}^{\mathrm{OC}}$ and $\mathbf{h}_{\mathrm{eff}}^{\mathrm{C}}$ are the corresponding dynamic fields. On the second member of Eq. (1) the first-order torque moments appear, viz. $\boldsymbol{\tau}=(\tau_\rho,\tau_\phi,\tau_z)$, respectively.

In order to give a realistic description of the spin dynamics taking into account both C and OC effects separately, we write the total dynamic magnetization by using the Heaviside step function $u(x)$. The total dynamic magnetization may thus be expressed by means of the relation $\mathbf{m}=u(\rho-a)\mathbf{m}_{\mathrm{OC}}+u(a-\rho)\mathbf{m}_{\mathrm{C}}$ with $u(\rho-a)=1(0)$ for $a<\rho\le R(0\le\rho<a)$ and $u(a-\rho)=1(0)$ for $0\le\rho<a(a<\rho\le R)$, where $a<R$ is the C radius. For $\rho=a$, that is at the boundary between the C and the OC regions, we use the convention according to which the discontinuity is eliminated, viz. $u(\rho-a)=u(a-\rho)=1/2$, and we have also $\mathbf{m}_{\mathrm{OC}}=\mathbf{m}_{\mathrm{C}}=\mathbf{m}$. In order to explain the above relation we consider the following two special cases: In the absence of a C region $(a=0)$ the static magnetization is in the dot plane so that $\mathbf{m}=\mathbf{m}_{\mathrm{OC}}$. On the other hand, assuming that the C region extends to the whole dot $(a=R)$, we get $\mathbf{m}=\mathbf{m}_{\mathrm{C}}$. Hence, this allows us to write $\mathbf{m}$ in terms of a combination of C and OC contributions for the general case where a C region of finite radius $a<R$ is present. The corresponding temporal evolution thus reads, $\frac{\partial \mathbf{m}}{\partial t}=u(\rho-a)\frac{\partial \mathbf{m}_{\mathrm{OC}}}{\partial t}+u(a-\rho)\frac{\partial \mathbf{m}_{\mathrm{C}}}{\partial t}$.

Equation (1) may in turn be expressed in terms of components as $-\frac{1}{\gamma}\frac{\partial m_\rho}{\partial t}=\tau_\rho$; $-\frac{1}{\gamma}[u(a-\rho)\frac{\partial m_\phi^{\mathrm{C}}}{\partial t}]=\tau_\phi$; and $-\frac{1}{\gamma}[u(\rho-a)\frac{\partial m_z^{\mathrm{OC}}}{\partial t}+u(a-\rho)\frac{\partial m_z^{\mathrm{C}}}{\partial t}]=\tau_z$. At this point one could solve the eigensystem problem by taking into account the above equations. Nevertheless, other approximations allow us to further simplify the solution. In particular, the τ_ϕ component may be neglected, because its OC contribution is substantially zero whereas its C contribution is smaller with respect to the other torque contributions. We may thus set $\frac{\partial m_\phi^{\mathrm{C}}}{\partial t}=0$. Furthermore, because of these approximations $\frac{\partial m_z}{\partial t}$ may be replaced by $\frac{\partial m_z^{\mathrm{OC}}}{\partial t}$. Hence, it is also possible to write $\frac{\partial \mathbf{m}}{\partial t}\simeq\frac{\partial \mathbf{m}_{\mathrm{OC}}}{\partial t}$. Equation (1) in the approximated form reads,

$$-\frac{1}{\gamma}\frac{\partial \mathbf{m}_{\mathrm{OC}}}{\partial t}=\tilde{\boldsymbol{\tau}}, \tag{2}$$

where the torque moments $\tilde{\boldsymbol{\tau}}=(\tau_\rho,\tau_z)$. Equation (2) gives a simplified description of spin dynamics because its temporal evolution is expressed in terms of the OC components m_ρ and m_z only, but at the same time it also includes the contribution of the C region in the torque moments. Notice that one may also derive Eq. (2) by using the η representation ($\eta=a/R$ is a weighting factor) described in Ref. 13.

In the calculation of the torque moments we suppose without loss of generality that the vortex chirality is $C=+1$ (i.e., counterclockwise rotation of the curling magnetization) and that the vortex polarity is $P=+1$ corresponding to upward orientation of the magnetization in the dot center with respect to the plane of the disk.

The effective static field reads $\mathbf{H}_{\mathrm{eff}}(\mathbf{r})=\mathbf{H}_{\mathrm{exch}}(\mathbf{r})+\mathbf{H}_{\mathrm{dem}}^{\mathrm{C}}(\mathbf{r})$. The first term on the second member is the static exchange field, while the latter is the C demagnetizing field. The perpendicular static demagnetizing field takes the form, $\mathbf{H}_{\mathrm{dem}}^{\mathrm{C}}(\mathbf{r})=[0,0,H_{\mathrm{dem}}^{\mathrm{C}}(\mathbf{r})]$, because the only "surface magnetic charges" are those generated by the static magnetization pointing outward or inward with respect to the dot surface in the C region. On the other hand, the isotropic static exchange field is given by $\mathbf{H}_{\mathrm{exch}}(\mathbf{r})=[0,H_{\mathrm{exch}}^{\phi}(\mathbf{r}),H_{\mathrm{exch}}^{z}(\mathbf{r})]$. The azimuthal dependence in $\mathbf{r}$ is only implicit in the cylindrical frame and the z component is different from zero in the C region only.

The dynamic effective field is $\mathbf{h}_{\mathrm{eff}}(\mathbf{r},t)=\mathbf{h}_d^{\mathrm{OC}}(\mathbf{r},t)+\mathbf{h}_d^{\mathrm{C}}(\mathbf{r},t)+\mathbf{h}_{\mathrm{exch}}(\mathbf{r},t)$, where the first term represents the OC dynamic dipolar magnetic field, the second term is the C dynamic dipolar field, and the latter is the isotropic dynamic-exchange field. These dynamic fields are spatially nonuniform. The dynamic dipolar magnetic field due to the "volume magnetic charges" is also called dynamic demagnetizing field and it is of magnetostatic origin. On the basis of the previous approximations on the dynamic magnetization also the isotropic dynamic-exchange field in the whole dot may thus be expressed in terms of the OC contribution only of the dynamic magnetization, i.e., $\mathbf{h}_{\mathrm{exch}}(\mathbf{r},t)\simeq\alpha\nabla^2\mathbf{m}_{\mathrm{OC}}(\mathbf{r},t)$ with $\alpha=2A/M_s^2$ the exchange constant and A being the exchange stiffness constant. Notice that this representation also takes indirectly into account the exchange contribution from the C

region and is in agreement with the fact that the exchange contribution is local.

Omitting the space and time dependences

$$\tilde{\boldsymbol{\tau}} = [M_s \sin\theta(h_{dz}^{\mathrm{OC}} + h_{dz}^{\mathrm{C}}) - M_s \cos\theta(h_{d\phi}^{\mathrm{OC}} + h_{d\phi}^{\mathrm{C}} + h_{\mathrm{exch}}^{\phi}) - H_{\mathrm{exch}}^{\phi} m_z \sin\theta - (H_{\mathrm{exch}}^{z} + H_{\mathrm{dem}}^{\mathrm{C}}) m_z \cos\theta + \alpha M_s \sin\theta \nabla^2 m_z]\hat{\boldsymbol{\rho}} - [M_s \sin\theta(h_{d\rho}^{\mathrm{OC}} + h_{d\rho}^{\mathrm{C}}) - H_{\mathrm{exch}}^{\phi} m_\rho + \alpha M_s \sin\theta \nabla^2 m_\rho]\hat{\mathbf{z}}.$$

Notice that the ρ component of the dynamic-exchange field represented in a compact form as $\alpha\nabla^2 m_\rho$ is given by $h_{\mathrm{exch}}^{\rho} = \alpha(\nabla^2 m_\rho - 1/\rho^2 m_\rho)$. However, the term proportional to $1/\rho^2$, if averaged over the OC area, turns out to be smaller than the first term and may be neglected. It is also $h_{\mathrm{exch}}^{\phi} = 2\alpha/\rho^2 \partial m_\rho/\partial\phi$. We have neglected $\tau_\phi = M_s \cos\theta(h_{d\rho}^{\mathrm{OC}} + h_{d\rho}^{\mathrm{C}}) - (H_{\mathrm{exch}}^{z} + H_{\mathrm{dem}}^{\mathrm{C}}) m_\rho$, which is very small with respect to the other contributions. The expression of $\tilde{\boldsymbol{\tau}}$ may be cast in a more simple form, because for dots exhibiting a vortex-state configuration, the C surface area $S_{\mathrm{C}} = \pi a^2$ is much smaller than the dot endface surface area $S = \pi R^2$. We get approximately $M_s \sin\theta \simeq M_s$ and $M_s \cos\theta \simeq 0$; the torque moment takes, thus, the simple form

$$\tilde{\boldsymbol{\tau}} \simeq [M_s(h_{dz}^{\mathrm{OC}} + h_{dz}^{\mathrm{C}}) - H_{\mathrm{exch}}^{\phi} m_z \sin\theta - (H_{\mathrm{exch}}^{z} + H_{\mathrm{dem}}^{\mathrm{C}}) m_z \cos\theta + \alpha M_s \nabla^2 m_z]\hat{\boldsymbol{\rho}} - [M_s(h_{d\rho}^{\mathrm{OC}} + h_{d\rho}^{\mathrm{C}}) - H_{\mathrm{exch}}^{\phi} m_\rho + \alpha M_s \nabla^2 m_\rho]\hat{\mathbf{z}}.$$

The torque term $-H_{\mathrm{exch}}^{\phi} m_z \sin\theta$ is in turn given by two contributions: in one appears the C contribution of H_{exch}^{ϕ} multiplied by $m_z \sin\theta$ in the C region and in the other the product between its OC contribution and the z component of the dynamic magnetization in the OC region given by m_z. Nevertheless, because of the negligible effect on the frequencies due to this assigning, in the derivation of the spectrum of spin modes, we have considered the single torque term $-H_{\mathrm{exch}}^{\phi} m_z \sin\theta$ leaving the θ dependence in the dynamic magnetization. The angular parts of the C dynamic magnetization components will be averaged over the C area only to obtain the spectrum of spin modes (see Sec. IV). In this way from each average one obtains a coefficient, which gives the weight of the spin mode amplitude in the whole dot. Finally, the torque term $-(H_{\mathrm{exch}}^{z} + H_{\mathrm{dem}}^{\mathrm{C}}) m_z \cos\theta$ is smaller with respect to the other terms appearing in τ_ρ, but we do not in principle neglect it. Indeed, by averaging $H_{\mathrm{exch}}^{z} + H_{\mathrm{dem}}^{\mathrm{C}}$ over the dot endface area separately from the angular part of the dynamic magnetization, the term $-(H_{\mathrm{exch}}^{z} + H_{\mathrm{dem}}^{\mathrm{C}}) m_z \cos\theta$ of τ_ρ results overestimated, but in this way the neglected term $-(H_{\mathrm{exch}}^{z} + H_{\mathrm{dem}}^{\mathrm{C}}) m_\rho$ of τ_ϕ is partially taken into account.

We write down the linearized equations of motion[13]

$$-M_s h_{d\rho} + H_{\mathrm{exch}}^{\phi} m_\rho - \alpha M_s \nabla^2 m_\rho = i\Omega m_z, \tag{3a}$$

$$-M_s h_{dz} + H_{\mathrm{exch}}^{\phi} m_z \sin\theta + (H_{\mathrm{exch}}^{z} + H_{\mathrm{dem}}^{\mathrm{C}}) m_z \cos\theta - \alpha M_s \nabla^2 m_z = -i\Omega m_\rho. \tag{3b}$$

Here $\Omega = \omega/\gamma$, $h_{d\rho} = h_{d\rho}^{\mathrm{OC}} + h_{d\rho}^{\mathrm{C}}$, and $h_{dz} = h_{dz}^{\mathrm{OC}} + h_{dz}^{\mathrm{C}}$.

One can consider different magnetization distributions to describe the dynamical properties in the vortex state. In particular, Usov and Peschany,[15] differently from other studies (see, e.g., Ref. 16), found a static magnetization distribution continuous for $\rho = a$ by means of a variational method. Furthermore, even though the results of the variational approach are compared with micromagnetic results in an elongated cylindrical particle of $0.50 \leq \beta \leq 10$, with the aspect ratio $\beta = L/R$, the derived magnetization distribution is more general and can be applied also to dots with $\beta < 0.50$ exhibiting a vortex-state configuration. Therefore, we choose from now on the Usov distribution given by $f(\rho) = 2a\rho/(a^2 + \rho^2)$ for $0 \leq \rho \leq a$ and $f(\rho) = 1$ for $a \leq \rho \leq R$, with $f(\rho) = \sin\theta(\rho)$.

Interestingly, one can derive quantitatively the equations of motion averaging the static magnetization over the dot endface area by means of the Usov distribution, viz. $M_s \langle \sin\theta(\rho) \rangle_{\theta(\rho)} = M_s[1 + \eta^2(3 - \pi)] \simeq M_s$ and $M_s \langle \cos\theta(\rho) \rangle_{\theta(\rho)} = M_s[\eta^2(2\ln 2 - 1)] \simeq 0$, respectively. $\langle \ldots \rangle_{\theta(\rho)}$ indicates the average by means of $\theta(\rho)$ over the dot endface area. Hence, $\tilde{\boldsymbol{\tau}}$ in view of the above averages reduces again to

$$\tilde{\boldsymbol{\tau}} \simeq [M_s(h_{dz}^{\mathrm{OC}} + h_{dz}^{\mathrm{C}}) - H_{\mathrm{exch}}^{\phi} m_z \sin\theta - (H_{\mathrm{exch}}^{cz} + H_{\mathrm{dem}}^{\mathrm{C}}) m_z \cos\theta + \alpha M_s \nabla^2 m_z]\hat{\boldsymbol{\rho}} - [M_s(h_{d\rho}^{\mathrm{OC}} + h_{d\rho}^{\mathrm{C}}) - H_{\mathrm{exch}}^{\phi} m_\rho + \alpha M_s \nabla^2 m_\rho]\hat{\mathbf{z}}.$$

Notice that each mode has a nonvanishing $h_{d\phi}^{\mathrm{C}}$ component, while only nonaxially symmetric modes have a $h_{d\phi}^{\mathrm{OC}}$ component. However, the corresponding torque contributions are negligible. Again the linearized equations of motion are found.

The main contribution to the static effective field is given by $\mathbf{H}_{\mathrm{exch}}(\mathbf{r}) = \alpha\nabla^2[0, M_\phi(\mathbf{r}), M_z(\mathbf{r})]$. Under the assumption that the static magnetization is uniform along z (Ref. 13), $\mathbf{H}_{\mathrm{exch}}(\mathbf{r}) = \mathbf{H}_{\mathrm{exch}}(\boldsymbol{\rho})$, where the ϕ dependence is implicit in the cylindrical reference frame. The ϕ component represented in a compact form as $\alpha\nabla^2 M_\phi(\boldsymbol{\rho})$ is given by $\alpha[\nabla^2 M_\phi(\boldsymbol{\rho}) - 1/\rho^2 M_\phi(\boldsymbol{\rho})]$. We get by taking into account the Usov distribution $H_{\mathrm{exch}}^{\phi}(\rho) = \pm \alpha M_s I(\rho)$, with $I(\rho) = [-\sin\theta(\frac{d\theta}{d\rho})^2 + \cos\theta\frac{d^2\theta}{d\rho^2} + \frac{1}{\rho}\cos\theta\frac{d\theta}{d\rho} - \frac{1}{\rho^2}\sin\theta]$ where both chiralities $C = \pm 1$ of the curling in-plane magnetization are taken into account ($C = -1$ indicates the in-plane component of the static magnetization rotates clockwise). Moreover, each spin mode should be affected by a different static exchange field such as for the demagnetizing field in saturated dots.[17] Nevertheless, we have found that each spin mode (with the only exception of the gyrotropic mode) is substantially affected by a static exchange field with the magnitude of the static exchange field averaged over the dot endface area $S = \pi R^2$. Hence $H_{\mathrm{exch}}^{\phi} = \pm \frac{\alpha M_s}{S} \int_S d^2\boldsymbol{\rho} I(\rho)$. Substituting $\theta(\rho) = \arcsin[2a\rho/(a^2 + \rho^2)]$ for $0 \leq \rho \leq a$, we get $I^{\mathrm{C}}(\rho) = -[16a^3\rho/(a^2 + \rho^2)^3]$. Instead for $a \leq \rho \leq R$ the quantity $I^{\mathrm{OC}}(\rho) = -4a^2/(a^2 + \rho^2)^2 - 1/\rho^2$ is obtained. The result of the average is, thus,

$$H_{\mathrm{exch}}^{\phi} = \mp 2\alpha M_s \frac{1}{R^2}\left[\ln\frac{1}{\eta} - \frac{1 - (1/\eta^2)}{1 + (1/\eta^2)} + \frac{\pi}{2}\right]. \tag{4}$$

One notes that the C term (the last term on the second member) differs slightly from the approximated one, derived in Ref. 13, because the factor π appears in place of three. Since the quantity inside square brackets is positive, the torque term arising from H_{exch}^{ϕ} causes a decrease in the spin mode energy in dots of radius in the nanometric range where the

exchange effects are not negligible. This effect is similar to that of the demagnetizing field in saturated systems. The first term on the second member showing a logaritmic dependence is a general result for vortex-state systems with cylindrical symmetry because it does not depend on the chosen magnetization distribution. Taking into account that $H_{\mathrm{exch}}^{z} = \mp 2\alpha M_s \frac{1}{R^2}$ (Ref. 13) where both polarities $P=\pm 1$ are taken into account ($P=-1$ corresponds to downward orientation in the dot center of the magnetization with respect to the plane of the disk), one finds that in the whole dot the static exchange field is antiparallel to $\mathbf{M}_0$. This behavior is very similar to that of the first-order demagnetizing field in perpendicularly saturated nonellipsoidal systems, which are antiparallel to the perpendicular static magnetization.

Another contribution to the C effective field is given by the perpendicular demagnetizing field $\mathbf{H}_{\mathrm{dem}}^{\mathrm{C}}(\mathbf{r}) = [0,0,H_{\mathrm{dem}}^{\mathrm{C}}(\mathbf{r})]$ generated by the surface magnetic charges in the C region. It is well known that the magnetostatic energy in the ultrathin dot limit becomes local and one can assume that the C region reduces to a point. However, in our model where dots of finite aspect ratio are studied the C region has a finite radius a. The average over z and z' yields to $H_{\mathrm{dem}}^{\mathrm{C}}(\boldsymbol{\rho})$. We have found that the contribution of $H_{\mathrm{dem}}^{\mathrm{C}}(\boldsymbol{\rho})$ on spin mode frequencies calculated by using the Usov distribution and averaged over $S=\pi R^2$ turns out to be for $R=100$ nm on average about one orders of magnitude smaller than the C part of the exchange field and it may thus be neglected.[13]

III. DIPOLAR MAGNETIC FIELDS

We restrict ourselves to the analysis of vortex spin modes in both the dipole-exchange and exchange regions that exhibit a surface character.[18] As shown by micromagnetic calculations, with increasing the dot thickness also modes showing nodes along z analogously to exchange perpendicular standing waves in continuous films may be present.[9] The trial solution taken for a single normal mode[1,7] in dots of nanometric and submicrometric size takes the general form $m_i(\rho,\phi,z) \propto [J_{|m|}(k\rho) - \sigma_m Y_{|m|}(k\rho)] e^{im\phi} e^{ik_{\perp} z}$, with $i=\rho,z$, $J_{|m|}(k\rho)(Y_{|m|}(k\rho))$ the Bessel function of the first (second) kind, σ_m the scattering amplitude and $m=0,\pm 1,\pm 2,\ldots$ as the azimuthal number. On the other hand, as shown in Ref. 11 for cylindrical dots with radii in the micrometric range where exchange effects may be considered negligible, it is realistic to assume as trial solution in response to a perpendicular magnetic tipping field $m_{\rho} \propto J_1(k\rho) e^{im\phi}$, with $m=0,1,2,\ldots$ for the whole set of modes. This choice has also been carried out by Guslienko *et al.*[19] studying the spin dynamics in thin cylindrical dots. Therefore, it is plausible to assume as trial eigenfunction of the $m=\pm 1$ and $n=0$ doublet $m_{\rho}(\rho,\phi,z) \propto [J_1(k\rho) - \sigma_{\pm 10} Y_1(k\rho)] e^{\pm\phi} e^{ik_{\perp} z}$ for the whole range of radii investigated.

In the vortex state the surface magnetic charges on the dot edges mostly contribute to the pinning of the in-plane radial component m_{ρ} only. The m_z component should be considered more realistically unpinned if its source of pinning is related to the surface magnetic charges on the dot lateral surface only. However, another important source of pinning of purely dipolar nature that can affect both the m_{ρ} and the m_z components in the vortex state arises from the volume magnetic charges related to the nonuniform dynamic dipolar field close to the dot edges.[19,20] Thus it is realistic to write the more general radial boundary condition in terms of components in the form: $\rho \frac{\partial m_i(\rho)}{\partial \rho} + p_i m_i(\rho)|_{\rho=R} = 0$, where the dependence of the magnetization from the indexes m and n has been omitted and $i=\rho,z$. In particular, $p_{\rho} = \Lambda + g(\beta)$ with $\Lambda = I_m (RL/2\pi l_0^2) \ln(4R/L)$, whereas $p_z = g(\beta)$. Here $l_0 = (A/2\pi M_s^2)^{1/2}$ is the reduced exchange length, $I_m = 2$ for $m=0$, $I_m = 1$ for $|m| \neq 0$, and $g(\beta)$ is a function of the aspect ratio $\beta = L/R$. The first term of p_{ρ}, Λ, is due to surface magnetic charges and represents the largest contribution, while the second term, $g(\beta)$, is caused by volume magnetic charges close to the edges. The term $g(\beta)$ not given explicitly increases with decreasing β such as for stripes in the saturated state.[20] From the radial boundary condition one finds the quantized in-plane wave number κ_{mn}, where $n=0,1,2,\ldots$ denotes the number of radial nodes. It is important to note that the above radial boundary condition is more strictly valid for thin dots because it was obtained in the limit of $\beta \ll 1$ (Refs. 1 and 20) and the calculated radial profiles of spin modes result in general pinned on the dot boundary. Nevertheless, from a more general point of view the m_{ρ} component must be strongly pinned also for dots of moderate aspect ratio to avoid the divergence of the magnetostatic energy on the boundary.[10] Instead, the m_z component should be considered for large β rather unpinned. Since the frequencies of spin modes with the only exception of the $m=0$ and $n=0$ mode at intermediate and large β (see Sec. V for a discussion) are substantially not affected by this different degree of pinning of the m_z component, we have assumed plausible for the numerical calculation the κ_{mn} determined for the m_{ρ} component also for the m_z component for each β studied. Moreover, in the numerical calculations on Py dots we have not accounted for $g(\beta)$, because at a given $\beta \ll 1$ is much smaller than Λ.

A. Dipolar magnetic fields with uniform magnetization along the thickness

In the first place we suppose that the profile of the dynamic magnetization is uniform along z, i.e., we take $\mathbf{m}(\mathbf{r}) = \mathbf{m}(\boldsymbol{\rho})$. This means that we examine thin dots, i.e., $L \ll R$. Therefore, it is also $\mathbf{h}_d(\mathbf{r}) = \mathbf{h}_d(\boldsymbol{\rho})$ with $\mathbf{h}_d(\boldsymbol{\rho}) = \mathbf{h}_d^{\mathrm{OC}}(\boldsymbol{\rho}) + \mathbf{h}_d^{\mathrm{C}}(\boldsymbol{\rho})$. As a result of this average, the $G_{\alpha z}$ and the $G_{z\beta}$ components of the Green's-function tensor $\hat{G}(\boldsymbol{\rho},\boldsymbol{\rho}')$, with $\alpha(\beta) = \rho,\phi$, vanish. The variable dynamic dipolar magnetic fields in their general form are defined as $\mathbf{h}_d^{\mathrm{OC}}(\boldsymbol{\rho}) = \int_{S_{\mathrm{OC}}} d^2\boldsymbol{\rho}' \hat{G}(\boldsymbol{\rho},\boldsymbol{\rho}') \mathbf{m}_{\mathrm{OC}}(\boldsymbol{\rho}')$ and $\mathbf{h}_d^{\mathrm{C}}(\boldsymbol{\rho}) = \int_{S_{\mathrm{C}}} d^2\boldsymbol{\rho}' \hat{G}^{\mathrm{C}}(\boldsymbol{\rho},\boldsymbol{\rho}') \mathbf{m}_{\mathrm{C}}(\boldsymbol{\rho}')$ for the OC and C region, respectively. In particular $\hat{G}^{\mathrm{C}}(\boldsymbol{\rho},\boldsymbol{\rho}') = \hat{R}^{-1} \hat{G}'(\boldsymbol{\rho},\boldsymbol{\rho}') \hat{R}$ with $\hat{R} = \hat{R}(\psi)$ ($\psi = \pi/2 - \theta$) the rotation matrix defined by the Euler angles $(0,\psi,0)$. $\hat{G}'$ is the tensorial Green's-function with respect to the rotated reference frame system, while $\hat{G}^{\mathrm{C}}$ is the rotated Green's-function tensor in the C region expressed with respect to the fixed OC reference frame (the ψ dependence is omitted). In explicit form,

$$\hat{G}^{\mathrm{C}}(\boldsymbol{\rho},\boldsymbol{\rho}') = \begin{bmatrix} G'_{\rho\rho} & G'_{\rho\phi}\sin\theta & G'_{\rho\phi}\cos\theta \\ G'_{\phi\rho}\sin\theta & G'_{\phi\phi}\sin^2\theta + G'_{zz}\cos^2\theta & (G'_{\phi\phi}-G'_{zz})\sin\theta\cos\theta \\ G'_{\phi\rho}\cos\theta & (G'_{\phi\phi}-G'_{zz})\sin\theta\cos\theta & G'_{\phi\phi}\cos^2\theta + G'_{zz}\sin^2\theta \end{bmatrix}, \tag{5}$$

omitting the dependence from $\boldsymbol{\rho}$ and $\boldsymbol{\rho}'$ in the second member. To calculate the spin mode spectrum, it is useful to give a simple definition of $\mathbf{h}_d^{\mathrm{C}}(\boldsymbol{\rho})$, namely, $\mathbf{h}_d^{\mathrm{C}}(\boldsymbol{\rho}) = \int_{S_{\mathrm{C}}} d^2\boldsymbol{\rho}' \langle \hat{G}^{\mathrm{C}}(\boldsymbol{\rho},\boldsymbol{\rho}') \rangle_{\theta(\rho)} \langle \mathbf{m}_{\mathrm{C}}(\boldsymbol{\rho}') \rangle_{\theta(\rho)}$, where here $\langle \cdots \rangle_{\theta(\rho)}$ denotes the average by means of $\theta(\rho)$ over the surface C area only. The numerical results derived by means of this definition are very close to those obtained with the general definition.

First, the integral over the azimuthal coordinate ϕ' appearing in $\mathbf{h}_d^{\mathrm{OC}}(\boldsymbol{\rho})$ and $\mathbf{h}_d^{\mathrm{C}}(\boldsymbol{\rho})$ by using the series expansion in Bessel functions of the Green's-function tensor components reads,

$$\int_0^{2\pi} e^{-il\phi'} e^{im\phi'} = 2\pi\delta_{lm}, \tag{6}$$

where l is the summand index of the Bessel series of the tensor Green's-function components. Due to the very complicated form of the solution close to the C region one can approximate the dynamic magnetization in the C region multiplying the solution found far from the vortex C region by $\sin\theta$. The dynamic dipolar magnetic fields given in the following are more strictly valid for radii ranging from the nanometric to the submicrometric range because they correspond to the most plausible choice of the trial radial eigenfunctions for dots of this size.

1. Axially symmetric modes

The integral of Eq. (6) does not vanish for $l=m$ so that for the axially symmetric modes ($m=0$ and n) only the $l=0$ summand in the tensorial Green's-function series expansion contributes. Correspondingly, the components of $\mathbf{h}_d^{\mathrm{OC}}(\rho)$ contributing to the linearized equations of motion may be expressed explicitly as

$$h_{di}^{\mathrm{OC}0n}(\rho) = -4\pi m_{0i}^{0n} \left\{ \int_a^R d\rho' \rho' [J_0(\kappa_{0n}\rho') + \sigma_{0n} Y_0(\kappa_{0n}\rho')] I_{ii}^0(\rho,\rho') \right\}, \tag{7}$$

with $i=\rho,z$. Instead, taking into account that the integral over ϕ' leads to a vanishing contribution of the $G'_{\rho\phi}$, $G'_{\phi\rho}$, and $G'_{\phi\phi}$ components to the nonlocal C dynamic dipolar magnetic field, we get

$$h_{di}^{\mathrm{C}0n}(\rho) = -4\pi m_{0i}^{0n} \left\{ A \int_0^a d\rho' \rho' [J_0(\kappa_{0n}\rho') + \sigma_{0n} Y_0(\kappa_{0n}\rho')] B I_{ii}^0(\rho,\rho') \right\}, \tag{8}$$

with $i=\rho,z$; $A=1$ for $i=\rho$ and $A=b+e$ for $i=z$; $B=\sin\theta(\rho')$ for $i=\rho$ and $B=1$ for $i=z$; and $b=(4\ln 2-2)(4-\pi)$ and $e=(2\pi-6)(2\ln 2-1)$. In particular, $I_{\rho\rho}^0(\rho,\rho') = \int_0^\infty dk k f(kL) J_1(k\rho) J_1(k\rho')$ and $I_{zz}^0(\rho,\rho') = \frac{1}{\rho'}\delta(\rho'-\rho) - \int_0^\infty dk k f(kL) J_0(k\rho) J_0(k\rho')$ with $f(kL) = 1 - \frac{1-e^{-kL}}{kL}$. The constants $(4\ln 2-2)$ and $(2\pi-6)$ are the result of the average over the C surface area by means of the Usov distribution of the angular parts $\sin^2\theta$ and $\sin\theta\cos\theta$ appearing in the rotated Green's-function tensor elements, respectively. Instead, the constants $(4-\pi)$ and $(2\ln 2-1)$ are the result of the same average of the angular parts $\sin\theta$ and $\cos\theta$ of the rotated dynamic magnetization, respectively. The term weighted by e is much smaller than the one weighted by b and has been thus neglected in the numerical calculations. $I_{\rho\rho}^0(\rho,\rho')$ and $I_{zz}^0(\rho,\rho')$ are calculated analytically in the Appendix [cf. Eqs. (A1)–(A4)]. Instead, we have numerically carried out the integrals over ρ'.

In the limit of thin dots ($R \gg L$) it is reasonable to apply the thin-film approximation. Strictly speaking the expressions of the approximated fields given in the following are derived by taking into account the radial dependence of the first term only, viz. $J_0(\kappa_{0n}\rho)$. As a matter of fact, the perturbative term given by $\sigma_{0n} Y_0(\kappa_{0n}\rho')$ is much smaller and does not affect the calculations. Substituting $I_{zz}^0(\rho,\rho')$ and taking into account that in the thin-film limit $R \gg L$, the z components of the dynamic dipolar field [cf. Eq. (8)] may be approximated by

$$h_{dz}^{\mathrm{OC}0n}(\rho) \simeq -4\pi m_{0z}^{0n} \left[\int_a^\infty d\rho' J_0(\kappa_{0n}\rho') \delta(\rho'-\rho) - \int_0^\infty dk k f(kL) J_0(k\rho) \int_a^\infty d\rho' \rho' J_0(k\rho') J_0(\kappa_{0n}\rho') \right]$$

and

$$h_{dz}^{\mathrm{C}0n}(\rho) \simeq -4\pi m_{0z}^{0n} b \left[\int_0^a d\rho' J_0(\kappa_{0n}\rho') \delta(\rho'-\rho) - \int_0^\infty dk k f(kL) J_0(k\rho) \int_0^a d\rho' \rho' J_0(k\rho') J_0(\kappa_{0n}\rho') \right]$$

for the OC and C regions, respectively. In particular, $\int_a^\infty d\rho' J_0(\kappa_{0n}\rho') \delta(\rho'-\rho) = u(\rho-a) J_0(\kappa_{0n}\rho)$; $u(\rho-a)$ is 1 for $a<\rho\leq R$ and 0 for $0\leq\rho<a$; hence, as expected, the

$h_{dz}^{\mathrm{OC}0n}(\rho)$ magnitude turns out to be zero in the C region. Taking into account the η representation used for the dynamic magnetization with $\eta=a/R$ the C weighting factor,[13] we may perform the substitution of $u(\rho-a)J_0(\kappa_{0n}\rho)$ with $(1-\eta)J_0(\kappa_{0n}\rho)$, where $(1-\eta)$ is a weighting factor for the OC region. The effect of this substitution is to reduce the OC magnitude of $h_{dz}^{\mathrm{OC}0n}(\rho)$ redistributing it into the C region. Moreover, by using the δ-function integral relation, we get

$$\int_a^\infty d\rho'\rho' J_0(k\rho')J_0(\kappa_{0n}\rho') = \int_0^\infty d\rho'\rho' J_0(k\rho')J_0(\kappa_{0n}\rho') - \int_0^a d\rho'\rho' J_0(k\rho')J_0(\kappa_{0n}\rho') = \frac{1}{\kappa_{on}}\delta(k-\kappa_{0n}) - \eta F(k,\kappa_{0n})$$

where

$$F(k,\kappa_{0n})=[kRJ_0(\kappa_{0n}a)J_1(ka)-\kappa_{0n}RJ_0(ka)J_1(\kappa_{0n}a)]/(k^2-\kappa_{0n}^2)$$

is an oscillating function. The expression on the second member has in turn to be integrated over k. The integration of the first term is trivial because $\int_0^\infty dkkf(kL)\frac{1}{\kappa_{0n}}\delta(k-\kappa_{0n})J_0(k\rho)=f(\beta\alpha_{0n})J_0(\kappa_{0n}\rho)$ with $\alpha_{0n}=\kappa_{0n}R$, while the integral $\eta\int_0^\infty dkkf(kL)F(k,\kappa_{0n})J_0(k\rho)$ may be carried out numerically. We have numerically calculated the corresponding approximated matrix elements evaluating the corresponding integrals under the reasonable assumption that $\kappa_{0n}\ll k$ (see the Appendix [cf. Eq. (A15)] for their general definition). On the basis of this calculation we have found that the result of the integration over k may be approximately substituted by the simple expression $\eta f(\beta\alpha_{0n})J_0(\kappa_{0n}\rho)$. In a similar way by using the, $u(a-\rho)$, Heaviside step function, we get the C component. These approximations allow us to write down $h_{dz}^{\mathrm{OC}0n}(\rho)$ and $h_{dz}^{\mathrm{C}0n}(\rho)$ in the following final form:

$$h_{dz}^{X0n}(\rho) \simeq -4\pi m_{0z}^{0n} b\xi_X[1-f(\beta\alpha_{0n})] \times[J_0(\kappa_{0n}\rho)+\sigma_{0n}Y_0(\kappa_{0n}\rho)], \tag{9}$$

where $X=\mathrm{OC},\mathrm{C}$, $\xi_X=1-\eta$ for $X=\mathrm{OC}$, and $\xi_X=\eta$ for $X=\mathrm{C}$. Here $b=1$ for $X=\mathrm{OC}$ and $b=(4\ln 2-2)(4-\pi)$ for $X=\mathrm{C}$. We have also added the term $\sigma_{0n}Y_0(\kappa_{0n}\rho)$ because of the very small value of σ_{0n}. This substitution is plausible because in addition to a good estimate of the exactly calculated matrix elements $d_{zz}^{\mathrm{OC}0n}$ and $d_{zz}^{\mathrm{C}0n}$ evaluated here in the thin dot limit it also gives an assigning of the dynamic dipolar energy density between the C and the OC regions very close to that obtained by means of the calculation of $d_{zz}^{\mathrm{OC}0n}$ and $d_{zz}^{\mathrm{C}0n}$.

One of the results of the thin-film approximation is represented by the quantization of the inverse dynamical susceptibility, i.e., $f(\beta\alpha_{0n})$. We use this result to make further strong approximations moving out of the integral over k the quantity $f(\beta\alpha_{0n})$ whose values are in the range between zero and one. This operation becomes more valid for dots of moderate β and for large α_{0n}, where $f(\beta\alpha_{0n})\to 1$. Therefore, from Eqs. (7) and (8) for $i=\rho$ taking into account the expression of $I_{\rho\rho}^0(\rho,\rho')$, we get

$$h_{d\rho}^{\mathrm{OC}0n}(\rho) \simeq -4\pi m_{0\rho}^{0n} f(\beta\alpha_{0n})\left\{\int_a^R d\rho'\rho'[J_0(\kappa_{0n}\rho') + \sigma_{0n}Y_0(\kappa_{0n}\rho')]\int_0^\infty dkkJ_1(k\rho)J_1(k\rho')\right\}$$

and

$$h_{d\rho}^{\mathrm{C}0n}(\rho) \simeq -4\pi m_{0\rho}^{0n} f(\beta\alpha_{0n})\left\{\int_0^a d\rho'\rho'[J_0(\kappa_{0n}\rho') + \sigma_{0n}Y_0(\kappa_{0n}\rho')]\sin\theta(\rho')\int_0^\infty dkkJ_1(k\rho)J_1(k\rho')\right\},$$

respectively. By using the property $\int_0^\infty dkkJ_1(k\rho)J_1(k\rho')=\frac{1}{\rho'}\delta(\rho'-\rho)$, we get, after an integration over ρ', $h_{d\rho}^{\mathrm{OC}0n}(\rho)\simeq -4\pi m_{0\rho}^{0n}u(\rho-a)f(\beta\alpha_{0n})J_0(\kappa_{0n}\rho)$ and $h_{d\rho}^{\mathrm{C}0n}(\rho)\simeq -4\pi m_{0\rho}^{0n}u(a-\rho)f(\beta\alpha_{0n})J_0(\kappa_{0n}\rho)\sin\theta(\rho)$.

The above equations are the expression of the local dipolar approximation for the radial components. Making a substitution similar to the one made for the z component they may be casted in the following final forms:

$$h_{d\rho}^{X0n}(\rho) \simeq -4\pi m_{0\rho}^{0n}\xi_X f(\beta\alpha_{0n})[J_0(\kappa_{0n}\rho)+\sigma_{0n}Y_0(\kappa_{0n}\rho)], \tag{10}$$

where the same final approximation has been performed such as for the case of the z component. The meaning of the symbols is the same as in Eq. (9). In Eq. (10) for $X=\mathrm{C}$, we have considered for the sake of simplicity the eigenfunction far from the vortex core ($\rho\gg a$) setting $\sin\theta=1$. Notice that the approximated corresponding matrix elements resulting from $h_{d\rho}^{\mathrm{OC}0n}(\rho)$ and $h_{d\rho}^{\mathrm{C}0n}(\rho)$ in Eq. (10) are $(1-\eta)f(\beta\alpha_{0n})$ and $\eta f(\beta\alpha_{0n})$, respectively, giving approximately the ratio between the C and OC dipolar energy density of the exact calculation. Indeed, the strong approximation consisting on the quantization of the inverse dynamical susceptibility is partially attenuated by substituting in the expression of the dipolar field radial C and OC components $u(\rho-a)$ and $u(a-\rho)$ with $(1-\eta)$ and η, respectively.

2. Nonaxially symmetric modes

According to the integral of Eq. (6) that gives a nonvanishing contribution for $l=m$, the components of the OC dynamic dipolar magnetic field of nonaxially symmetric modes ($|m|\neq 0,n$), which contribute to the linearized equations of motion are given by

$$h_{di}^{\mathrm{OC}mn}(\rho,\phi) = -4\pi m_{0i}^{mn}\left\{\int_a^R d\rho'\rho'[J_{|m|}(\kappa_{mn}\rho') - \sigma_{mn}Y_{|m|}(\kappa_{mn}\rho')]I_{ii}^m(\rho,\rho')\right\}e^{im\phi}, \tag{11}$$

with $i=\rho,z$. Instead, we write the C components in the form:

$$h_{d\rho}^{\mathrm{C}mn}(\rho,\phi) = -4\pi m_{0\rho}^{mn} C e^{im\phi}, \tag{12a}$$

$$h_{dz}^{\mathrm{C}mn}(\rho,\phi) = -4\pi\{m_{0\rho}^{mn}\tilde{e}D - m_{0z}^{mn}[(e-\tilde{f})E-(e+b)F]\}e^{im\phi}, \tag{12b}$$

where $\tilde{e}=(2\ln 2-1)$ and $\tilde{f}=(3-4\ln 2)(4-\pi)$. The constant $(3-4\ln 2)$ is the result of the average over the C surface by means of the Usov distribution of the angular part $\cos^2\theta$. Here

$$C = \int_{\epsilon}^{a} d\rho'\rho'[J_{|m|}(\kappa_{mn}\rho') - \sigma_{mn}Y_{|m|}(\kappa_{mn}\rho')] \times \sin\theta(\rho')I_{\rho\rho}^{m}(\rho,\rho'),$$

$$D = \int_{\epsilon}^{a} \rho' d\rho'[J_{|m|}(\kappa_{mn}\rho') - \sigma_{mn}Y_{|m|}(\kappa_{mn}\rho')]I_{\phi\rho}^{m}(\rho,\rho'),$$

$$E = \int_{\epsilon}^{a} \rho' d\rho'[J_{|m|}(\kappa_{mn}\rho') - \sigma_{mn}Y_{|m|}(\kappa_{mn}\rho')]I_{\phi\phi}^{m}(\rho,\rho'),$$

$$F = \int_{\epsilon}^{a} \rho' d\rho'[J_{|m|}(\kappa_{mn}\rho') - \sigma_{mn}Y_{|m|}(\kappa_{mn}\rho')]I_{zz}^{m}(\rho,\rho').$$

In particular,

$$I_{\rho\rho}^{m}(\rho,\rho') = \int_{0}^{\infty} dkkf(kL)J_{m}'(k\rho)J_{m}'(k\rho'),$$

$$I_{\phi\rho}^{m}(\rho,\rho') = i\int_{0}^{\infty} dkkf(kL)\tfrac{m}{k\rho}J_{m}(k\rho)J_{m}'(k\rho'),$$

$$I_{\phi\phi}^{m}(\rho,\rho') = \int_{0}^{\infty} dkkf(kL)\tfrac{m}{k\rho}J_{m}(k\rho)\tfrac{m}{k\rho'}J_{m}(k\rho'),$$

and

$$I_{zz}^{m}(\rho,\rho') = \tfrac{1}{\rho'}\delta(\rho'-\rho) - \int_{0}^{\infty} dkkf(kL)J_{m}(k\rho)J_{m}(k\rho'),$$

respectively. It is also $I_{\rho\rho}^{m}(\rho,\rho')=I_{\rho\rho}^{-m}(\rho,\rho')$, $I_{\phi\rho}^{m}(\rho,\rho')=[I_{\phi\rho}^{-m}(\rho,\rho')]^{*}$, $I_{\phi\phi}^{m}(\rho,\rho')=I_{\phi\phi}^{-m}(\rho,\rho')$, and $I_{zz}^{m}(\rho,\rho')=I_{zz}^{-m}(\rho,\rho')$, with ϵ as an infinitesimal quantity which permits to exclude the $Y_{|m|}$ singularity at $\rho=0$. In the following numerical calculations we take into account in the second member of Eq. (12b) only the term weighted by the prefactor b that is proportional to $I_{zz}^{m}(\rho,\rho')$ because it is much larger than the other terms. The integrals $I_{\rho\rho}^{m}(\rho,\rho')$ and $I_{zz}^{m}(\rho,\rho')$ for $m=\pm 1,\pm 2\ \ldots$ are calculated analytically in the Appendix A [cf. Eqs. (A5)–(A14)].

Again, we apply the local dipolar approximation to the $h_{dz}^{\mathrm{OC}mn}$ and $h_{dz}^{\mathrm{C}mn}$ given in Eq. (11) for $i=z$ and Eq. (12b) in the limit of thin dots ($R\gg L$) assumimg $\sigma_{mn}\ll 1$. We get

$$h_{dz}^{\mathrm{OC}mn}(\rho,\phi) \simeq -4\pi m_{0z}^{mn}\left[\int_{a}^{\infty} d\rho' J_{m}(\kappa_{mn}\rho')\delta(\rho'-\rho) - \int_{0}^{\infty} dkkf(kL)J_{m}(k\rho)\int_{a}^{\infty} d\rho'\rho' J_{m}(k\rho') \times J_{m}(\kappa_{mn}\rho')\right]e^{im\phi}$$

and for the C contribution

$$h_{dz}^{\mathrm{C}mn}(\rho,\phi) \simeq -4\pi m_{0z}^{mn}b\left[\int_{0}^{a} d\rho' J_{m}(\kappa_{mn}\rho')\delta(\rho'-\rho) - \int_{0}^{\infty} dkkf(kL)J_{m}(k\rho)\int_{0}^{a} d\rho'\rho' J_{m}(k\rho') \times J_{m}(\kappa_{mn}\rho')\right]e^{im\phi}.$$

Analogously to the case of axially symmetric modes we use the δ-function integral relation

$$\int_{0}^{\infty} d\rho'\rho' J_{m}(k\rho')J_{m}(\kappa_{mn}\rho') = \tfrac{1}{\kappa_{mn}}\delta(k-\kappa_{mn})$$

to calculate

$$\int_{a}^{\infty} d\rho'\rho' J_{m}(k\rho')J_{m}(\kappa_{mn}\rho') = \int_{0}^{\infty} d\rho'\rho' J_{m}(k\rho')J_{m}(\kappa_{mn}\rho') - \int_{0}^{a} d\rho'\rho' J_{m}(k\rho')J_{m}(\kappa_{mn}\rho') = \tfrac{1}{\kappa_{mn}}\delta(k-\kappa_{mn}) - \eta F(k,\kappa_{mn})$$

where $F(k,\kappa_{mn})=[\kappa_{mn}RJ_{m-1}(\kappa_{mn}a)J_{m}(ka) - kRJ_{m-1}(ka)J_{m}(\kappa_{mn}a)]/(k^2-\kappa_{mn}^2)$ is an oscillating function. Carrying on the same steps made for the axially symmetric modes for the calculation of the corresponding dipolar matrix elements in the limit for $\kappa_{mn}\ll k$, the integral over k of the oscillating function, namely,

$$\eta\int_{0}^{\infty} dk\, kf(kL)F(k,\kappa_{mn})J_{m}(k\rho)$$

can be approximately substituted by $\eta f(\beta\alpha_{mn})J_{m}(\kappa_{mn}\rho)$ with $\alpha_{mn}=\kappa_{mn}R$. Thus, we get in the general form;

$$h_{dz}^{Xmn}(\rho,\phi) \simeq -4\pi m_{0z}^{mn}b\xi_{X}[1-f(\beta\alpha_{mn})][J_{|m|}(\kappa_{mn}\rho) - \sigma_{mn}Y_{|m|}(\kappa_{mn}\rho)]e^{im\phi}, \tag{13}$$

providing that the perturbative term $\sigma_{mn}Y_{|m|}(\kappa_{mn}\rho)$ is included. The meaning of the symbols is the same as in Eq. (9). Consequently, taking into account the $f(\beta\alpha_{mn})$ quantization, the OC and C ρ components may be written as

$$h_{d\rho}^{\mathrm{OC}mn}(\rho,\phi) \simeq -4\pi m_{0\rho}^{mn}f(\beta\alpha_{mn})T^{\mathrm{OC}}e^{im\phi}, \tag{14a}$$

$$h_{d\rho}^{\mathrm{C}mn}(\rho,\phi) \simeq -4\pi m_{0\rho}^{mn}f(\beta\alpha_{mn})T^{\mathrm{C}}e^{im\phi}, \tag{14b}$$

where

$$T^{\mathrm{OC}} = \int_a^R \rho' d\rho' [J_{|m|}(\kappa_{mn}\rho') - \sigma_{mn} Y_{|m|}(\kappa_{mn}\rho')] \times \int_0^\infty dk\, k J'_m(k\rho) J'_m(k\rho')$$

and

$$T^{\mathrm{C}} = \int_\epsilon^a \rho' d\rho' [J_{|m|}(\kappa_{mn}\rho') - \sigma_{mn} Y_{|m|}(\kappa_{mn}\rho')] \times \sin\theta(\rho') \int_0^\infty dk\, k J'_m(k\rho) J'_m(k\rho').$$

One sees that the radial components given in Eqs. (14a) and (14b) have yet a nonlocal dependence from the corresponding radial components of the dynamic magnetization. The approximated Eqs. (13), (14a), and (14b) are valid for $|m| \neq 0$ and $n=0$ modes with the exception of the gyrotropic mode whose amplitude is mainly represented by the Bessel function of the second kind. From the exact calculation of the dipolar diagonal matrix elements, one should consider more generally $\eta=(a/R)^t$ with $t>1$ for modes with $|m| \geq 1$ and n. Finally, the local dipolar approximation progressively fails with increasing β because the static magnetization close to the dot edges is no longer on the dot plane perpendicular to the cylinder axis.

Expressions similar to those given above for the dipolar magnetic fields of axially and nonaxially symmetric modes in dots of radii in the micrometric range can be found. One should take into account that for dots of this size the more plausible trial radial eigenfunctions assume the form $\propto J_1(\kappa_n) e^{im\phi}$, with $m=0, \pm 1, \pm 2, \ldots$ (Ref. 11). Straightforwardly, one could also find the expressions of the corresponding dipolar fields within the local dipolar approximation.

B. Dipolar magnetic fields with nonuniform magnetization along the thickness

It is well known far back by use of micromagnetic calculations that the static magnetization is nonuniform along the dot thickness, especially in dots of moderate aspect ratio (see, e.g., Ref. 21 and references cited therein). This nonuniformity is present also in the OC region and may affect the mode profiles, which are also nonuniform along z (as also shown by our micromagnetic calculations on cylindrical dots). It is reasonable to assume a surface character of the spin modes studied here including the $|m| \neq 0$ and n modes because of their radial character despite their backwardlike "volume" nature related to the azimuthal wave number $k_\phi = \pm 1, \pm 2, \ldots$ (Refs. 7, 8, and 13). In order to find the z component of the wave number for each spin mode and to simply calculate it we use, in analogy to the case of the continuous film,[18] the differential equation of the magnetostatic potential ψ. This equation is derived in the absence of an external field and neglecting the exchange effects from the linearized equations of motion and from the Maxwell equations in the magnetostatic limit. ψ gives rise to the dynamic dipolar magnetic field $\mathbf{h}$. Substituting into the potential differential equation the trial solution ψ in cylindrical coordinates yields $\kappa_\perp^{mn} \simeq \pm i\kappa_{mn}$, where $\kappa_\perp^{mn}$ is the perpendicular quantized wave number, which modes have a surface character. Without loss of generality we assume for the whole set of modes $\kappa_\perp^{mn} = \pm i\kappa_{mn}$. We do not take into account the quantization of the perpendicular wave vector resulting more important in the C region. This further quantization effect would be obtained applying the "mixed" exchange boundary condition and would be related to pinning effects on the dot endfaces. Also the twisting configuration of the static magnetization along z, which becomes more important with increasing L in nanometric dots, can contribute to the pinning of the mode profiles close to the upper and lower dot endfaces. The twisting effect could be included in the "mixed" exchange boundary condition along z. It would give, under the reasonable assumption that the pinning effects affect equally the modes, a quantization of the same order of magnitude for each mode of the spectrum at fixed thickness and a surface character to the spin excitations investigated in this study. However, it would be, in principle, more difficult to treat quantitatively. We thus consider plausible for the calculations the simple quantized relation with the equality, i.e., $\kappa_\perp^{mn} = \pm i\kappa_{mn}$, which is a purely dipolar result and gives, in principle, a different $\kappa_\perp^{mn}$ for each mode.

The general expression of the OC dynamic dipolar magnetic field reads $\mathbf{h}_d^{\mathrm{OC}}(\mathbf{r}) = \int_{V_{\mathrm{OC}}} d^3\mathbf{r}' \hat{G}(\mathbf{r},\mathbf{r}') \mathbf{m}(\mathbf{r}')$, whereas the C contribution is $\mathbf{h}_d^{\mathrm{C}}(\mathbf{r}) = \int_{V_{\mathrm{C}}} d^3\mathbf{r}' \hat{G}^{\mathrm{C}}(\mathbf{r},\mathbf{r}') \mathbf{m}_{\mathrm{C}}(\mathbf{r}')$. Analogously to the case of uniform magnetization along z, one may express the C contribution in the form $\mathbf{h}_d^{\mathrm{C}}(\mathbf{r}) = \int_{V_{\mathrm{C}}} d^3\mathbf{r}' \langle \hat{G}^{\mathrm{C}}(\mathbf{r},\mathbf{r}') \rangle_{\theta(\rho)} \langle \mathbf{m}_{\mathrm{C}}(\mathbf{r}') \rangle_{\theta(\rho)}$. V_{OC} and V_{C} are the OC and C volumes, respectively.[13] The meaning of the other symbols is the same as in the case of uniform magnetization. In order to overcome the restriction due to the local dipolar approximation[13] in the present approach one distinguishes between the k dependence resulting from the Fourier momentum representation of the magnetostatic tensorial Green's-function and the κ_{mn} dependence of the spin modes. Choosing the reference frame origin in the half plane between the two endfaces of the dot, we thus evaluate the quantity $\int_{-L/2}^{L/2} dz \int_{-L/2}^{L/2} dz' e^{-\kappa_{mn}(L/2+z')} e^{-k|z-z'|} e^{-\kappa_{mn}(L/2+z)} / \int_{-L/2}^{L/2} dz e^{-2\kappa_{mn}(L/2+z)} = 2/kf(kL, \beta\alpha_{mn})$, where

$$f(kL,\beta\alpha_{mn}) = \frac{kL}{k^2L^2 - \beta^2\alpha_{mn}^2} \left\{ \frac{\beta\alpha_{mn}}{\sinh(\beta\alpha_{mn})} - e^{kL}[\beta\alpha_{mn} \coth(\beta\alpha_{mn}) - kL] \right\} e^{-kL} \quad (15)$$

depends upon k and κ_{mn}. The factor proportional to $e^{-\kappa_{mn}(L/2+z)}$ expresses the attenuation along z of a spin mode going from the lower endface to the upper endface after the substitution $\kappa_\perp^{mn} = \pm i\kappa_{mn}$. The result of Eq. (15) is also obtained by using the factor proportional to $e^{-\kappa_{mn}(L/2-z)}$ that gives the attenuation along the thickness of a spin mode going from the upper to the lower endface. The quantity $f(kL, \beta\alpha_{mn})$ is the most general expression of the inverse

dynamical susceptibility for the case of nonuniform magnetization. The interval of variation of $f(kL,\beta\alpha_{mn})$ is between zero and one for a given $\kappa_{mn}\neq 0$ and $f(kL,\beta\alpha_{mn})\rightarrow f(kL)$ for $\kappa_{mn}\rightarrow 0$, that is tends to the inverse dynamical susceptibility of the uniform case. From Eq. (15) one can derive straightforwardly the corresponding form of the inverse dynamical susceptibility in the framework of the local dipolar approximation. In order to do this one substitutes the wave vector k of the Fourier representation of the Green's-function with the quantized wave number κ_{mn} obtaining $\chi(\beta\alpha_{mn})=\lim_{k\rightarrow\kappa_{mn}} f(kL,\beta\alpha_{mn})=\beta\alpha_{mn}\frac{e^{-2\beta\alpha_{mn}}}{(e^{-2\beta\alpha_{mn}}-1)}+\frac{1}{2}$. For intermediate aspect ratios, that is in the range between small and moderate aspect ratios and for moderate aspect ratio $(\beta<1)$ $\chi(\beta\alpha_{mn})$ may be fitted by $\chi_f(\beta\alpha_{mn})=\frac{1-e^{-2\beta\alpha_{mn}}}{2}$(Ref. 13). However, the function $\chi_f(\beta\alpha_{mn})$ violates the ultrathin limit because for $L\ll R$ it tends to $\beta\alpha_{mn}$ and not to $\beta\alpha_{mn}/2$ showing a different behavior with respect to that of $\chi(\beta\alpha_{mn})$. Moreover, both $\chi(\beta\alpha_{mn})$ and $\chi_f(\beta\alpha_{mn})$ suffer from the same restriction, which is their range of variation between zero and 1/2.

In order to get the components of the dipolar magnetic field under the assumption of nonuniform magnetization along z, one first substitutes in Eqs. (7) and (8) for $m=0$ and n modes and in Eqs. (11), (12a), and (12b) for $|m|\neq 0$ and n modes $f(kL)$ with $f(kL,\beta\alpha_{mn})$. In this way the matrix elements evaluated numerically $\bar{I}_{\rho\rho}$ and $\bar{I}_{zz}$ (see the Appendix) appear in place of $I_{\rho\rho}$ and I_{zz}. The corresponding simpler expressions obtained within the local dipolar approximation may be derived following the same calculations performed for the case of uniform magnetization along z. We get Eqs. (9) and (10) for $m=0$ and n modes and Eqs. (13), (14a), and (14b) for $|m|\neq 0$ and n modes with $\chi(\beta\alpha_{mn})$ in place of $f(\beta\alpha_{mn})$. By using the fitted $\chi_f(\beta\alpha_{mn})$ in place of $\chi(\beta\alpha_{mn})$, we obtain the dynamic dipolar magnetic fields found by Zivieri and Nizzoli.[13]

IV. SPIN DYNAMICS

Following the same steps given in Ref. 13 the spin modes quantized spectrum can be expressed as

$$\Omega_{mn}^2=\Omega_M^2[\xi\alpha_{mn}^2+\tilde{h}_{\mathrm{exch}}^{\phi}-d_{\rho\rho}^{mn}][\xi\alpha_{mn}^2+\tilde{h}_{\mathrm{exch}}^{\phi}g+\tilde{h}_{\mathrm{exch}}^{z}s-d_{zz}^{mn}], \tag{16a}$$

where $\Omega_M=4\pi M_s$, $\xi=\alpha/4\pi R^2$, $\tilde{h}_{\mathrm{exch}}^{\phi}=H_{\mathrm{exch}}^{\phi}/\Omega_M$, $\tilde{h}_{\mathrm{exch}}^{z}=H_{\mathrm{exch}}^{z}/\Omega_M$, $d_{\rho\rho}^{mn}=d_{\rho\rho}^{\mathrm{OC}mn}+d_{\rho\rho}^{\mathrm{C}mn}$ and $d_{zz}^{mn}=d_{zz}^{\mathrm{OC}mn}+d_{zz}^{\mathrm{C}mn}$, $g=4-\pi$, and $s=2\ln 2-1$. Here g and s are the result of the average over the C area of the angular parts $\sin\theta$ and $\cos\theta$, respectively of the rotated z component of the dynamic magnetization in the C region by means of the Usov distribution. $n=0,1,2,\ldots$ denotes the number of radial nodes of axially and nonaxially symmetric modes (with the exception of the gyrotropic mode) corresponding to the zeros of the radial boundary condition. Notice that the $n=0$ radial mode number corresponds to the $n=1$ of other formalisms[1,11,19,22] and the different classification extends to the successive radial mode numbers. Furthermore, in numbering the radial nodes of the radial profiles the node close to $\rho=0$ is not taken into account. The diagonal matrix elements of the dynamic dipolar magnetic field $d_{ii}^{\mathrm{OC}mn}=d_{ii}^{\mathrm{OC}mn}(\beta\alpha_{mn})$, $d_{ii}^{\mathrm{C}mn}=d_{ii}^{\mathrm{C}mn}(\beta\alpha_{mn})$ with $i=\rho,z$ for the case of uniform magnetization along z have been calculated exactly and their expressions are given in the Appendix [cf. Eq. (A15)]. These elements are substituted by the corresponding ones, namely $\bar{d}_{ii}^{\mathrm{OC}mn}=\bar{d}_{ii}^{\mathrm{OC}mn}(\beta\alpha_{mn})$, $\bar{d}_{ii}^{\mathrm{C}mn}=\bar{d}_{ii}^{\mathrm{C}mn}(\beta\alpha_{mn})$ with $\bar{d}_{ii}^{mn}=\bar{d}_{ii}^{\mathrm{OC}mn}+\bar{d}_{ii}^{\mathrm{C}mn}$ with $i=\rho,z$ derived for the case of nonuniform magnetization along z {see the Appendix [cf. Eq. (A21)]}.

Within the local dipolar approximation the diagonal matrix elements $d_{\rho\rho}^{mn}$ $(\bar{d}_{\rho\rho}^{mn})$, $d_{zz}^{mn\mathrm{OC}}$ $(\bar{d}_{zz}^{mn\mathrm{OC}})$, and $d_{zz}^{mn\mathrm{C}}$ $(\bar{d}_{zz}^{mn\mathrm{C}})$ are substituted by the inverse dynamical susceptibility and weighted by the C and OC η and $(1-\eta)$ factors to get

$$\tilde{\Omega}_{mn}^2=\Omega_M^2[\xi\alpha_{mn}^2+\tilde{h}_{\mathrm{exch}}^{\phi}+\lambda(\beta\alpha_{mn})\mathrm{C}_{mn}]\times\{\xi\alpha_{mn}^2+\tilde{h}_{\mathrm{exch}}^{\phi}g+\tilde{h}_{\mathrm{exch}}^{z}s+[1-\lambda(\beta\alpha_{mn})][(1-\eta)+b\eta]\}, \tag{16b}$$

with $\lambda(\beta\alpha_{mn})=f(\beta\alpha_{mn})$ for the case of uniform magnetization and $\lambda(\beta\alpha_{mn})=\chi(\beta\alpha_{mn})$ for the case of nonuniform magnetization. In the calculations we have also used the fitted $\chi_f(\beta\alpha_{mn})$. Equation (16b)with $\lambda(\beta\alpha_{mn})=\chi_f(\beta\alpha_{mn})$ is very similar to Eq. (11) of Ref. 13. C_{mn} are coefficients given in the Appendix [cf. Eq. (A16)]. In particular, for axially symmetric modes $(m=0,n)$, we get $\mathrm{C}_{0n}=1$ for each n setting $\mathrm{C}_{0n}=\mathrm{C}_0=1$. For nonaxially symmetric modes $(|m|\neq 0,n)$ we set $\mathrm{C}_{mn}=\mathrm{C}_m$ for $n=0$. Furthermore, the dynamic-exchange terms appearing in Eqs. (16a) and (16b) would not be exactly equal to $\xi\alpha_{mn}^2$ for radii in the micrometric range where the in-plane eigenfunctions are $\propto J_1(\kappa_n\rho)e^{im\phi}$, but for this size the dynamic exchange is negligible. For dots of radius varying on the micrometric scale $(R\gg L)$ Eq. (16a) may be further simplified. Indeed, not only the exchange contributions are negligible but also d_{zz}^{mn} approach one and $d_{\rho\rho}^{mn}$ can be expressed in the ultrathin dot limit so that $\Omega_{mn}\propto\Omega_M(\beta\alpha_{mn}/2)^{1/2}$. In other words $\Omega_{mn}\propto\sqrt{L/R}$ as already found in literature.[3,7,11,19]

The frequencies of the gyrotropic vortex mode (also called fundamental gyrotropic mode in three-dimensional ferromagnets[21]) due to the gyrotropic precession of C can be found from Eq. (16) and from the solution of the radial boundary condition with the smallest quantized wave number. The frequencies are less than 1 GHz and for very small aspect ratios are approximately proportional to L/R in agreement with the results of recent models.[7,19] Its in-plane profile is mainly confined in the C region and has a simple structure along z with no nodes. This mode was not found in this range of frequencies in our previous study[13] because the frequencies calculation of spin modes was done within the local dipolar approximation resulting not valid for the gyrotropic mode.

A. Frequency splitting of $\pm|m|$ and n modes

Let us derive quantitatively the frequency splitting $\Delta\Omega_{\mp mn}$ of the $\pm|m|$ and n doublets from Eq. (16a). As the static exchange field contributes equally for both modes of the doublets, we neglect their corresponding torque terms in the derivation of the frequency splitting. This yields to the following simple approximated formula of the frequency splitting:

$$\Delta\Omega^2_{\mp|m|n} = \Omega^2_M(\omega_{-|m|n} - \omega_{+|m|n})^2, \tag{17a}$$

with

$$\omega^2_{\mp|m|n} = [d^{\mp|m|n}_{zz} d^{\mp|m|n}_{\rho\rho} - (d^{\mp|m|n}_{zz} + d^{\mp|m|n}_{\rho\rho})\xi(\alpha_{\mp|m|n})^2 + \xi^2(\alpha_{\mp|m|n})^4]. \tag{17b}$$

For dots of $\beta > 0.20$ the matrix elements $\bar{d}_{\rho\rho}$ and $\bar{d}_{zz}$ would appear in Eq. (17b) in place of $d_{\rho\rho}$ and d_{zz}. One singles out three dynamic contributions to the splitting. The first one may be ascribed to the dipolar term only and is given by both its C and OC contributions. The second term is a mixed term due to the coupling of the contributions of the dipolar and dynamic-exchange fields and the last one is represented by the dynamic-exchange field only. In particular, we study the splitting of the $m = \pm 1$ and $n = 0$ doublets because for this couple of modes experimental measurements are available. The main source of frequency splitting is due to the terms proportional to the dynamic dipolar magnetic fields of the doublets, but also the corresponding dynamic-exchange fields give their contribution especially for radii in the nanometric range. The more the scattering amplitude $\sigma_{\mp 10}$ is large, the more $d^{-10}_{\rho\rho}$ and $d^{+10}_{\rho\rho}$ $[\xi(\alpha_{-10})^2$ and $\xi(\alpha_{+10})^2]$ have different values and the more the splitting is important. While $d^{\mp 10}_{ii}$ with $i = \rho, z$ depend on the aspect ratio β, the $\xi(\alpha_{\mp 10})^2$ terms substantially depend on the inverse power of R^2. This means that, for a fixed aspect ratio β obtained with different R (and different L), the splitting is larger when R is in the nanometric range and submicrometric range because of the non-negligible contribution of the nonuniform dynamic-exchange term. Moreover, the rate of decrease in the splitting with increasing R is weaker because the calculated $m = \pm 1$ and $n = 0$ frequency splittings are yet non-negligible for radius R in the micrometric range as also confirmed by experimental measurements with time-resolved Kerr microscopy (TRKM) (Refs. 7 and 14). On the other hand, the splitting corresponding to $|m| > 1$ and n nonaxially symmetric modes is one orders of magnitude smaller for dots with radius ranging in the nanometric scale. This smaller value is due to the fact that modes of each $\pm|m| > 1$ and n doublet have very close dynamic magnetic field contributions. It is worth noting that the doublet splitting of the nonaxially symmetric modes can also be interpreted in terms of a Berry phase of magnons.

The underestimation of the frequency splitting of the $m = \pm 1$ and $n = 0$ doublet in Ref. 13 was due to the assumption of the same radial dipolar contribution given by $\chi_f(\beta\alpha_{\pm 10})C_1$ with the same coefficient C_1 for both modes and to the dependence of the scattering amplitudes $\sigma_{\pm 1}$ from l_0 in place of R_0 (see the next section for the definition of R_0).

V. RESULTS

In the numerical calculations we have used the parameters fitted to results of the continuous Py film:[23] $4\pi M_s = 9.5$ kG, $\gamma/2\pi = 2.996$ GHz/kOe, and $\alpha/4\pi = 2.42 \times 10^{-13}$ cm^2. These parameters are slightly different from those used in literature. However, we have found that the numerical discrepancy on the mode frequencies is at maximum of about 5%.

In order to study the effect of C on spin dynamics, we have chosen as scattering amplitude $\sigma_m = \sigma_m(kR_0)$ in place of $\sigma_m = \sigma_m(kl_0)$, where $R_0 = (2A)^{1/2}/M_s$ plays the role of an exchange length (not to be confused with l_0). The quantity R_0, for the range of thicknesses investigated, is much larger than l_0 and is of the order of the C radius a. One could, in principle, choose $\sigma_m = \sigma_m(ka)$ with the C radius a defined as the value for which $M_z(\rho = a) = 0$ on the two endfaces neglecting the bottleneck effect[24] present in dots of moderate aspect ratio $\beta < 1$. However, this choice suffers from the limitation that a is not a constant of the magnetic material but has a weak dependence from the dot thickness. With the parameters used, we get for Py $R_0 = 18$ nm. Because of the small difference between the analytical and micromagnetic distribution in the peripheral C region where the latter exhibits a larger tail, we have used the C radius determined by means of a micromagnetic approach. We have thus set $a = 18$ nm for $L < 50$ nm and $a = 26$ nm for $L \geq 50$ nm (notice the slight different value used here for small thicknesses with respect to Ref. 13). Finally, for a ranging between 18 and 26 nm, the ratio between the C and OC exactly calculated dipolar matrix elements does not substantially vary.

1. Frequencies of the spin modes

In Fig. 1 the frequencies vs β of the $m = 0$, $n = 0$ mode (the fundamental mode F) and of the $m = 0$, $n = 1$ mode for uniform magnetization along z are depicted. This mode gives, in general (but not always), the largest contribution to the calculated scattering cross section, and in the BLS measurements it corresponds often to the highest peak. Its profile is mainly confined in the OC region and results pinned on the dot border. It may be considered analogous in the vortex state of the resonant mode in the saturated state.[17,25] Due to the underestimation of the dipolar matrix element the approximated F mode frequencies (dotted line) are downshifted with respect to the exactly calculated ones (solid line) for the whole range of aspect ratios investigated, and the discrepancy between the two curves is already 15% at small aspect ratios and slightly increases with increasing β. The disagreement becomes more important for moderate and large aspect ratios ($\beta < 1$) where also the thin-film approximation does not hold anymore. Moreover, the approximated frequencies show a maximum at $\beta = 0.50$ and then slightly monotonically decrease. Instead, the exactly calculated frequencies have a maximum shifted toward higher aspect ratios ($\beta > 0.80$). This general trend is due to the increase in $d^{00}_{\rho\rho}$ (in modulus) and to the decrease in d^{00}_{zz} (in modulus) with β and leads to a deviation from the linear dependence behavior from $\sqrt{\beta}$ typical of dots with very small aspect ratios. Also the dynamic-exchange term contributes in part to the deviation from the simple $\sqrt{\beta}$ dependence as already found for cylindrical dots of $\beta > 0.15$ (Ref. 7). Finally, notice that the m_z component of the F mode results rather unpinned for $\beta > 0.30$ leading to a slight downshift of the corresponding frequencies.

In panel (b) one sees that the exactly calculated frequencies for nonuniform magnetization along z (solid line) increase at low aspect ratios reach a maximum at about $\beta = 0.50$ and then decrease. Instead, the approximated frequencies (dotted and short-dotted lines, respectively) monotoni-

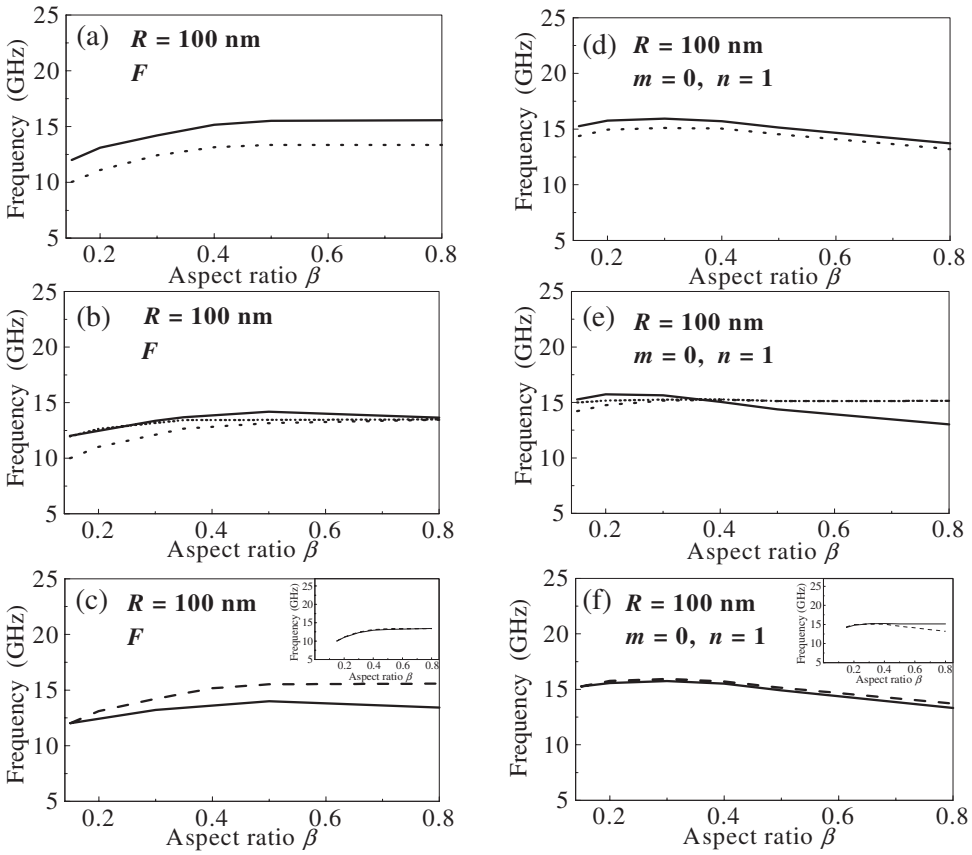

FIG. 1. Panel (a): Solid line: frequency behavior of the F mode vs β for $R=100$ nm derived by means of Eq. (16a) for uniform magnetization. Dotted line: the same but according to Eq. (16b) with $f(\beta\alpha_{00})$. Panel (b): Solid line: as in panel (a) but for nonuniform magnetization. Dotted line: the same but obtained from Eq. (16b) with $\chi(\beta\alpha_{00})$. Short-dotted line: the same but with $\chi_f(\beta\alpha_{00})$. Panel (c): Solid line: frequency behavior of the F mode vs β for $R=100$ nm according to Eq. (16a) with nonuniform magnetization. Dashed line: the same but with uniform magnetization. Inset: Solid line: the same but using Eq. (16b) with $\chi(\beta\alpha_{00})$. Dashed line: the same but with $f(\beta\alpha_{00})$. Panel (d): as in panel (a) but for the $m=0$ and $n=1$ modes. Panel (e): as in panel (b) but for the $m=0$ and $n=1$ modes. Panel (f): as in panel (c) but for the $m=0$ and $n=1$ mode.

cally increase and become constant at high β. At low β the calculation performed using $\chi(\beta\alpha_{00})$ largely underestimates the exact value (more than 15%), while at intermediate β both frequency curves are lower than the exact one (more than 7%). Finally, at large aspect ratios the approximated frequency curves merge asymptotically toward the exact one. Indeed, the quantities $\chi(\beta\alpha_{00})[1-\chi(\beta\alpha_{00})]$ and $\chi_f(\beta\alpha_{00})[1-\chi_f(\beta\alpha_{00})]$ converge toward an asymptotic value at large β leading to the asymptotic behavior of the frequencies. As the profile along z of the m_z component of the F mode is almost uniform especially in the OC region and with increasing β, the corresponding matrix element $\bar{d}_{zz}^{00}$ is equal to d_{zz}^{00}, which is in turn very close to the static demagnetizing factor N_{zz}.

In panel (c) the exactly calculated frequencies according to Eq. (16a) are compared. The effect of the z dependence becomes progressively more important for $\beta>0.20$. At high aspect ratios the gap between the two frequency curves is remarkable (about 14% for $\beta=0.80$) because of the lower value of $\bar{d}_{\rho\rho}^{00}$ with respect to $d_{\rho\rho}^{00}$ with increasing β. The calculation shows that the neglected twisting effect on the static magnetization and the formation of asymmetric domain walls along z, especially in the C region, not only affects the gyrotropic modes[9,21] but is indirectly and partially taken into account also in the F mode dynamics. This effect contributes in part to the important frequency downshift of the F mode found for nonuniform magnetization along z in dots of large β. For the sake of comparison in the inset to panel (c) the calculated frequencies determined by means of the local dipolar approximation are also displayed. Also within the approximated calculation the z dependence leads to a downshift of the F mode frequencies. Nevertheless, this effect for intermediate and large β is masked by the asymptotic behavior of the function $\chi(\beta\alpha_{00})[1-\chi(\beta\alpha_{00})]$.

Similar conclusions may be drawn for the $m=0$ and $n=1$ mode frequencies [panels (d)–(f)] even though the underestimation effects due to the local dipolar approximation are less pronounced (on average about 5%). Also the effect of the z dependence for $\beta>0.25$ causes a downshift of the frequencies that is on average of only 3%. The weight of the C effective field, assuming the yet valid quantized wave number obtained from the radial boundary condition of the standard dot, on the frequencies of the F and the $m=0$ and $n=1$ modes, respectively, is calculated by neglecting in Eq. (16a), the corresponding $d_{\rho\rho}^{Cmn}$ and d_{zz}^{Cmn} [cf. Eq. (A15)] or $\bar{d}_{\rho\rho}^{Cmn}$ and $\bar{d}_{zz}^{Cmn}$ [cf. Eq. (A21)] together with the C contribution of the static exchange field. For $R=100$ nm the C effect for both uniform and nonuniform magnetizations along z

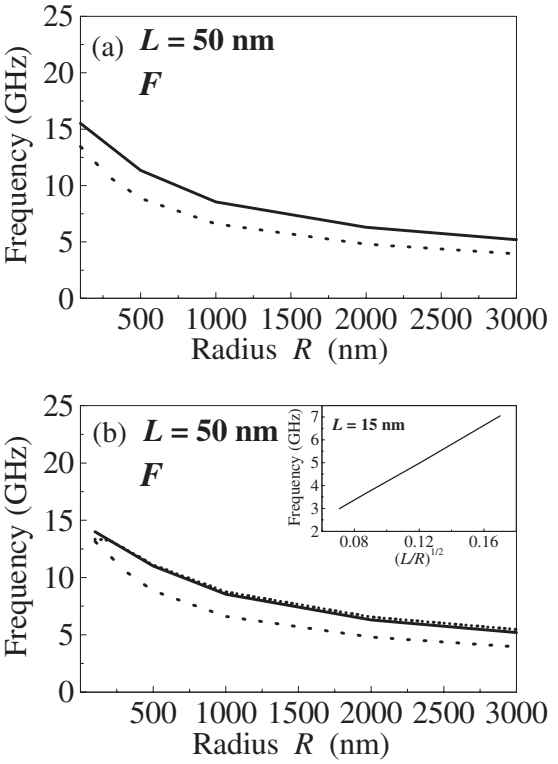

FIG. 2. Panel (a): Solid line: frequency behavior of the F mode vs R for $L=50$ nm obtained according to Eq. (16a) for uniform magnetization along z. Dotted line: the same but according to Eq. (16b) with $f(\beta\alpha_{00})$. Panel (b): Solid line: as in panel (a) but for nonuniform magnetization along z. Dotted line: the same but using Eq. (16b) with $\chi(\beta\alpha_{00})$. Short-dotted line: the same but using Eq. (16b) with $\chi_f(\beta\alpha_{00})$. Inset: frequency behavior of the F mode vs $\sqrt{\beta}$ for $L=15$ nm.

turns out to be about 20% and is for the F mode about 5% smaller than the one estimated within the local dipolar approximation.[13]

The frequency behavior of the F mode vs R is displayed in Fig. 2. The same effects due to the local dipolar approximation discussed for the frequencies vs β are present here, both considering uniform and nonuniform magnetization along z. In the inset to panel (b) one sees that, in the ultrathin dot limit $L \ll R$, the frequencies of the F mode calculated according to Eq. (16a) are proportional to $\sqrt{\beta}$ (Refs. 3, 7, 11, and 14). The calculation has been done by using as radial eigenfunction for the F mode a form proportional to $J_0(\kappa_{00}\rho)+\sigma_{00}Y_0(\kappa_{00}\rho)$, but one would have obtained the same frequency behavior (with slightly different frequencies) by using a form proportional to $J_1(\kappa_0\rho)$.

Figure 3 displays the frequency behavior of the $m=\pm 1$ and $n=0$ couple of modes as a function of β. The general effect of the approximated calculation (dotted line) is the underestimation of the exactly calculated frequencies for the whole range of β (on average about 8% at small β and about 5% at large β) due to the underestimation of the matrix elements $d_{\rho\rho}^{\pm 10}$ [see panel (a)]. Apart from that the approximated frequencies present a maximum at $\beta \simeq 0.40$ reproducing the qualitative trend of the exactly calculated ones.

In panel (b) the same comparison is displayed for nonuniform magnetization along z. The behavior of the frequencies

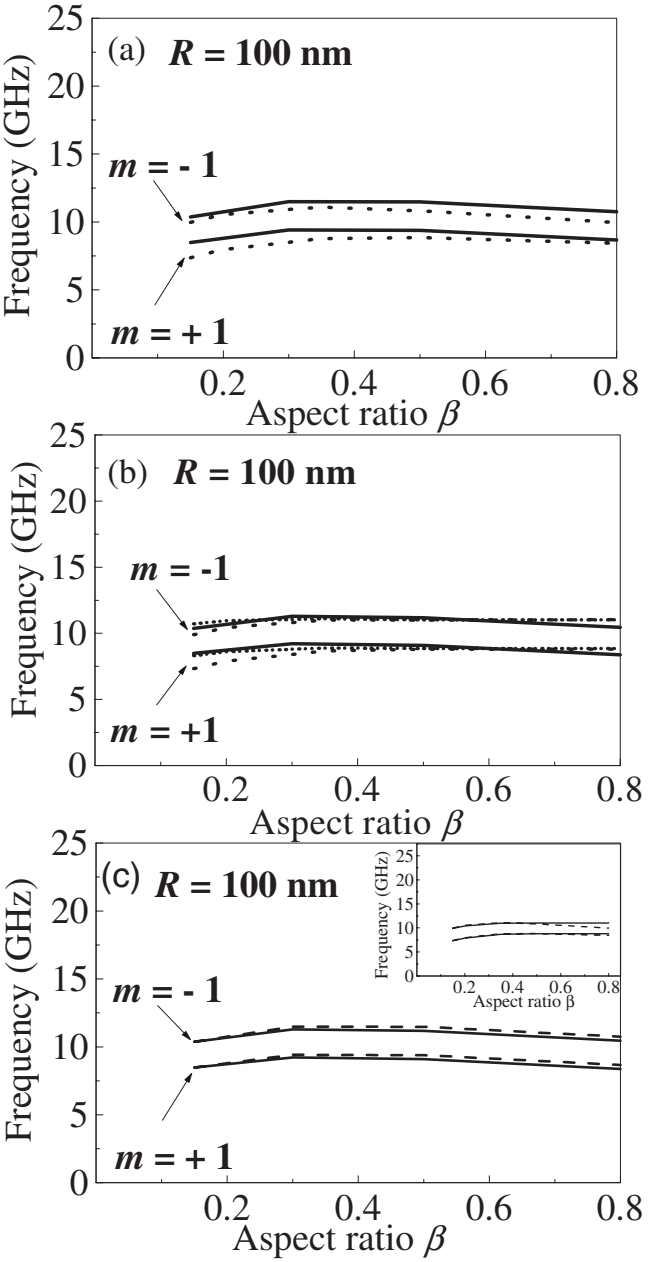

FIG. 3. Panel (a): Solid lines: frequency behavior for $R=100$ nm of the $m=\pm 1$ and $n=0$ modes vs β derived by means of Eq. (16a) for uniform magnetization along z. Dotted lines: the same but according to Eq. (16b) with $f(\beta\alpha_{\pm 10})C_{\pm 1}$. Panel (b): Solid lines: as in panel (a) but for nonuniform magnetization. Dotted lines: the same but obtained from Eq. (16b) by use of $\chi(\beta\alpha_{\pm 10})C_{\pm 1}$. Short-dotted lines: the same but with $\chi_f(\beta\alpha_{\pm 10})C_{\pm 1}$. Panel (c): Solid lines: frequency behavior for $R=100$ nm of the $m=\pm 1$ modes vs β according to Eq. (16a) for nonuniform magnetization along the thickness. Dashed lines: the same but for uniform magnetization along z. Inset: Solid lines: frequency behavior of the $m=\pm 1$ and $n=0$ modes vs β using Eq. (16b) with $\chi(\beta\alpha_{\pm 10})C_{\pm 1}$. Dashed line: the same but with $f(\beta\alpha_{\pm 10})C_{\pm 1}$.

can be understood on the basis of the same arguments previously presented for the axially symmetric modes. In both approximated calculations shown in panels (a) and (b), we have found $C_{+1}=0.40$ and $C_{-1}=0.57$ according to Eq. (A16)

for the whole range of thicknesses investigated. Due to the divergence of the Bessel function of the second kind $Y_{\pm 1}$ for $\rho \to 0$, a careful calculation of the coefficients $C_{\pm 1}$ is needed. Hence, we have determined $C_{\pm 1}$ by averaging, when carrying out the ρ' integration, the value obtained dividing the numerator in the second member of Eq. (A16) evaluated for $\epsilon \simeq a$ by the integral over ρ in the denominator for zero (but yet finite) and the one calculated evaluating both the numerator and the integral over ρ at the denominator for $\epsilon \simeq a$. A similar procedure has been followed for the calculation of the $d_{\rho\rho}^{\pm 10}$ and $\bar{d}_{\rho\rho}^{\pm 10}$ matrix elements to obtain the exact frequencies. The C_{+1} is equal to that found in Ref. 13 that was nevertheless obtained via a different calculation. Indeed, due to the smaller degree of divergence of $\sigma_{10}(\kappa_{10} l_0) Y_1(\kappa_{10}\rho)$, only the value for $\epsilon \simeq 0$ (with $\epsilon \to 0$ in that case) was calculated. Finally, the error in the calculation of the $m = \pm 1$ and $n=0$ mode frequencies caused by the local dipolar approximation is less pronounced with respect to that of the F mode frequencies for dots of nanometric size.

Quantitatively the downshift of the frequencies obtained for nonuniform magnetization is of the order of 3% as shown in panel (c). In the inset to panel (c) the same comparison is shown taking into account the local dipolar approximation. Conclusions similar to the case of axially symmetric modes may be drawn for the $m = \pm 1$ and $n=0$ doublet. Finally, the C effect for $R=100$ nm calculated in the same way as done for the axially symmetric modes is more pronounced on the $m=-1$ and $n=0$ mode frequencies because of its larger scattering amplitude. The average effect on the two frequencies of the doublet is about 10% for dots of radius $R=100$ nm and thickness $L<50$ nm, where $a=18$ nm and slightly larger (about 14%) for $L \geq 50$ nm. This result is the same both for uniform magnetization and for nonuniform magnetization along z, and the C effect is on average more than 10% smaller than the one derived within the local dipolar approximation.[13]

In Fig. 4 we show the frequencies of the $m = \pm 1$ and $n=0$ modes vs R at $L=50$ nm. One sees that by using $\chi_f(\beta\alpha_{\pm 10}) C_{\pm 1}$ [short-dotted line in panel (b)], an overestimation of the exactly calculated frequencies especially for $R > 200$ nm is present due to the violation of the ultrathin dot limit. The gap between the $m = \pm 1$ and $n=0$ mode frequencies obtained within the local dipolar approximation [cf. Eq. (16b)] in both panels (a) and (b) is smaller, with increasing the radius R, than the one derived within the exact calculation [cf. Eq. (16a)]. In the inset to panel (b) it is shown that, in the ultrathin dot limit $L \ll R$, also the frequencies of the $m=+1$ and $n=0$ modes are proportional to $\sqrt{\beta}$. The frequencies of the $m=-1$ and $n=0$ modes (not shown) have a similar behavior. In order to better evaluate the effect of the C region for dots of $R \geq 500$ nm and thickness $L=50$ nm ($\beta \leq 0.10$), we have considered for the calculation of $d_{\rho\rho}^{\pm 10}$ and $\bar{d}_{\rho\rho}^{\pm 10}$ equivalent dots of fixed radius $R=100$ nm with the same aspect ratio β. Even though it may lead to a slight overestimation of the frequency splitting this approach is reasonable because the dipolar matrix elements depend on β. Moreover, in this way it is also assumed that the quantitative effect of the scattering amplitude $\sigma_{\pm 10}$ on the matrix elements is the same for fixed β. In the calculation of the frequencies the scattering amplitude, which enters in the determination of the quantized wave number has then been evaluated in correspondence of the effective radius.

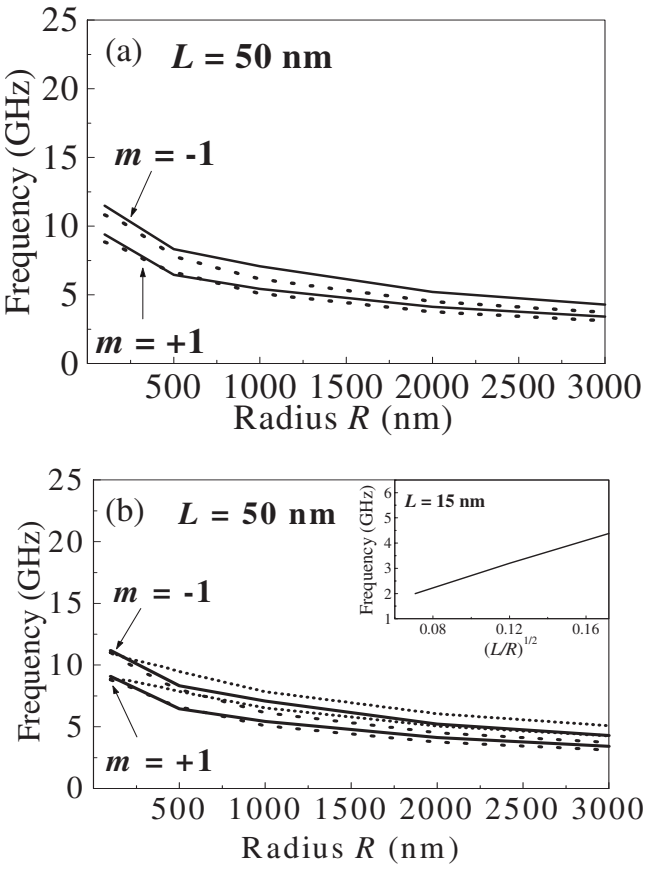

FIG. 4. Panel (a): Solid lines: frequency behavior of the $m = \pm 1$ and $n=0$ modes vs R for $L=50$ nm obtained with Eq. (16a) for uniform magnetization along the thickness. Dotted lines: the same but according to Eq. (16b) with $f(\beta\alpha_{\pm 10}) C_{\pm 1}$. Panel (b): Solid lines: as in panel (a) but for nonuniform magnetization along the thickness. Dotted lines: the same but using Eq. (16b) with $\chi(\beta\alpha_{\pm 10}) C_{\pm 1}$. Short-dotted lines: the same but with $\chi_f(\beta\alpha_{\pm 10}) C_{\pm 1}$. Inset: frequency behavior of the $m=+1$ mode vs $\sqrt{\beta}$ for $L = 15$ nm.

In Fig. 5, panel (a) the radial profile of the modulus of the ϕ component of the static exchange field $H_{\text{exch}}^{\phi}(\rho)$ is shown for a Py dot of radius $R=100$ nm and thickness $L=50$ nm where the effect of the static exchange field on spin modes frequencies is non-negligible. The ϕ component of the exchange field vanishes for $\rho=0$, reaches a maximum in the C region at about one half of the C radius, and then progressively reduces in the OC region to converge asymptotically to zero on the dot border. In panel (b) for the sake of comparison we show the profile of the corresponding modulus of the z component $H_{\text{exch}}^{z}(\rho)$ of the static exchange field.

In panel (c) the exactly calculated frequencies of the F mode (solid line) are compared with the ones obtained neglecting the static exchange contribution to the torque in Eq. (16a) (dotted line). The effect is an upshift of the frequencies on average of about 5% for the whole range of β investigated. The dash-dotted curve results from the calculation carried out neglecting both the static exchange contribution and

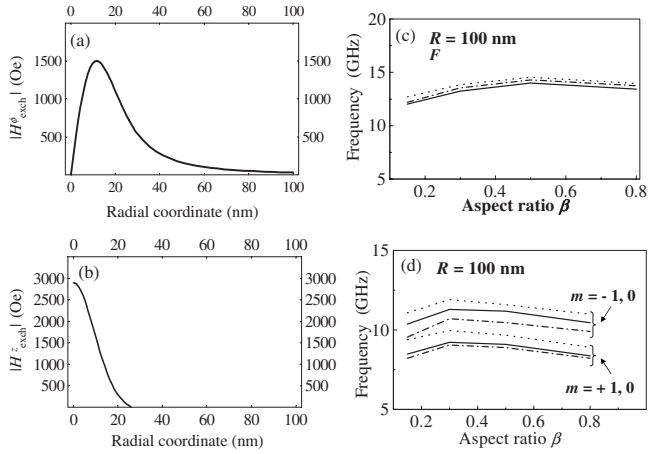

FIG. 5. Panel (a): radial profile of $|H^{\phi}_{\mathrm{exch}}(\rho)|$ for a dot of radius $R=100$ nm and thickness $L=50$ nm. Panel (b): corresponding radial profile of $|H^{z}_{\mathrm{exch}}(\rho)|$. Panel (c): frequencies of the F mode vs β. Solid line: exactly calculated frequencies by means of Eq. (16a) for nonuniform magnetization. Dotted line: calculated frequencies obtained neglecting the static exchange contribution to the torque in Eq. (16a). Dash-dotted line: calculated frequencies obtained neglecting both the static and the nonuniform dynamic exchange contributions to the torque in Eq. (16a). Panel (d): as in panel (c) but for the frequencies of the $m=\pm 1$ and $n=0$ modes.

the nonuniform dynamic exchange to the torque in Eq. (16a). One notes that the obtained frequencies overestimate the exactly calculated ones of about 2%. This means that for the F mode frequencies the effect of the dynamic-exchange torque is almost totally counterbalanced by the static exchange torque.

For the $m=-1$ and $n=0$ mode frequencies, the upshift obtained neglecting the static exchange contribution to the torque [see panel (d)] is on average of 5% for the whole range of thicknesses, while the upshift of the $m=+1$ and $n=0$ mode frequencies is more accentuated at small β (about 10%) and reduces at large thicknesses (about 6%). Instead, when one neglects both the static and the dynamic nonuniform exchange contributions to the torque the frequency curves of the doublet are clearly downshifted with respect to the exactly calculated ones showing an opposite behavior with respect to the F mode. In particular, for the $m=-1$ and $n=0$ modes, this downshift is about 8% at small β and about 5% at large β. The same effect is smaller for the $m=+1$ and $n=0$ modes whose downshift is on average about 2%. Indeed the nonuniform exchange contribution of the $m=\pm 1$ and $n=0$ modes to the torque is larger than the corresponding one of the F mode. The quantitative effect of the static exchange field on the frequencies of the $m=0$ and $n\neq 0$ modes and of the $m=\pm 1$ and $n\neq 0$ modes is very close to the one derived for the F mode and to that of the $m=\pm 1$ and $n=0$ modes, respectively. This is true also for the $|m|>1$ and n modes. Instead, if one neglects both the static- and dynamic-exchange field the quantitative effect is different for the different modes due to the different dynamic-exchange contributions.

In Fig. 6 we show the frequency behavior of the most representative $\pm|m|$ and $n=0$ doublets with $|m|=2,3$, respec-

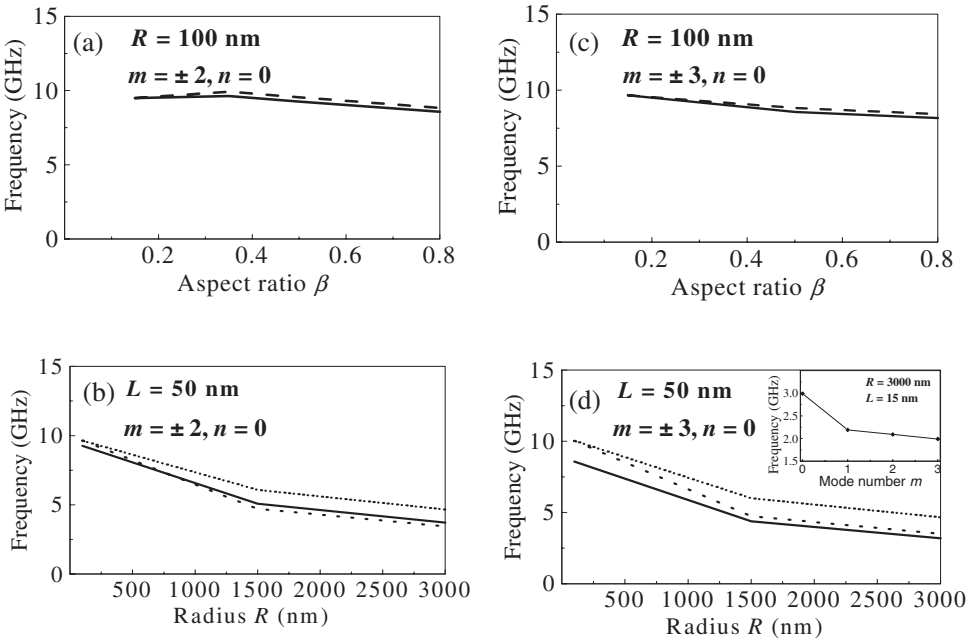

FIG. 6. Panel (a): Solid lines: frequencies the $m=\pm 2$ and $n=0$ modes vs β according to Eq. (16a) with nonuniform magnetization along the thickness. Dashed lines: the same but with uniform magnetization along z. Panel (b): Solid lines: frequency behavior of the $m=\pm 2$ and $n=0$ modes vs R for $L=50$ nm determined by means of Eq. (16a) with nonuniform magnetization along z. Dotted line: the same but obtained from Eq. (16b) by use of $\chi(\beta\alpha_{\pm 20})\mathrm{C}_{\pm 2}$. Short-dotted lines: the same but using $\chi_f(\beta\alpha_{\pm 20})\mathrm{C}_{\pm 2}$. Panel (c): as in panel (a) but for the $m=\pm 3$ and $n=0$ modes. Panel (d): as in panel (b) but for the $m=\pm 3$ and $n=0$ modes. Inset: frequency behavior as a function of the azimuthal mode number m for $R=3000$ nm and $L=15$ nm.

tively. The calculated frequency splitting of the $m=\pm 2$ and $n=0$ modes is small (less than 0.1 GHz) and of the same orders of magnitude as the one calculated by Ivanov and Zaspel[12] for the $m=\pm 2$ doublet. Conclusions analogous to the case of the $m=\pm 1$ and $n=0$ doublets on the quantitative effect of the z dependence of the dynamic magnetization may be drawn for the $m=\pm 2$, $n=0$, and $m=\pm 3$, $n=0$ frequencies, respectively [panels (a) and (c)]. Also the effect of the local dipolar approximation on the frequencies compared to the exact calculation [panels (b) and (d)] show the same limitations found for the $m=\pm 1$ and $n=0$ doublet for $R \gg L$. The frequency calculation in panel (b) and (d) is less detailed for R in the submicrometric range because we were interested to show the general behavior of the frequencies of the $m=\pm 2$ and $n=0$, and $m=\pm 3$ and $n=0$ modes for R ranging from nanometric to micrometric size. Moreover, for the $m=\pm 3$ and $n=0$ frequencies the local dipolar approximation seems to cause a larger overestimation of the exact calculations with respect to the $m=\pm 1$, $m=\pm 2$ and $n=0$ doublets. We are reminded that, due to convergence problems present for $|m| \geq 3$ modes, we have extrapolated the $d_{\rho\rho}^{\pm 30}$ and $\bar{d}_{\rho\rho}^{\pm 30}$ matrix elements from the behavior of $d_{\rho\rho}^{\pm|m|0}$ and $\bar{d}_{\rho\rho}^{\pm|m|0}$ for $|m| \leq 2$ for uniform and nonuniform magnetization, respectively. In the inset to panel (d) we show for a dot of radius $R=3000$ nm and thickness $L=15$ nm the frequency behavior as a function of the mode number m for $m=0,1,2,3$ and $n=0$ calculated according to Eq. (16a) for uniform magnetization along z. The frequencies for $m \neq 0$ correspond to the mean values of the frequencies of the $\pm|m|$ doublets. Since we were interested in the qualitative behavior of the frequencies we have used as corresponding radial eigenfunctions in the calculations the form proportional to $J_{|m|}(\kappa_{m0}\rho) - \sigma_{m0} Y_{|m|}(\kappa_{m0}\rho)$, but one would have obtained a similar result (with small differences in the corresponding frequencies) by using the more plausible form proportional to $J_1(\kappa_0 \rho)$. One sees the typical negative dispersion of frequency for $m \neq 0$ modes due to the behavior of the dipolar term when the exchange effects are negligible as found by Buess *et al.*[4,11]

In order to determine the coefficients C_m with $m=\pm 2, \pm 3, \pm 4, \pm 5$, we have used the unperturbed radial eigenfunctions $J_{|m|}(\kappa_{m0}\rho)$ in Eq. (A16) because $\sigma_{\pm m} \ll \sigma_{\pm 1}$ (Ref. 1). Hence, also $C_{+m}=C_{-m}=C_m$ and $C_{+3}=C_{-3}=C_3$. The obtained numerical values turn out to be $C_2=0.37$, $C_3=0.31$, $C_4=0.27$, and $C_5=0.24$, respectively for each β. One notes that C_2 and C_3 (C_4 and C_5) are larger than 0.10 (0.12) with respect to the ones given in Ref. 13, but we believe that these higher values may be regarded as more realistic because they have been calculated, avoiding the numerical problems related to the Y_m divergence for $\rho \to 0$, which are difficult to treat.[13] The quantitative effect on the corresponding frequencies of the discussed doublets caused by the larger calculated C_m is an upshift of the frequencies of about 1 GHz with respect to the ones calculated in Ref. 13. Finally, the weight of the C region on the $\pm|m|$ and $n=0$ frequencies with $|m|>1$ is smaller with respect to the one on the $\pm|m|=1$ doublet for a dot of radius $R=100$ nm because of the smaller value of the corresponding scattering amplitudes and can be considered almost negligible. It is important to note that the real C effect on the spin modes can be evaluated removing the C region such as the case of rings where also the splitting of nonaxially symmetric modes is not present anymore.[14]

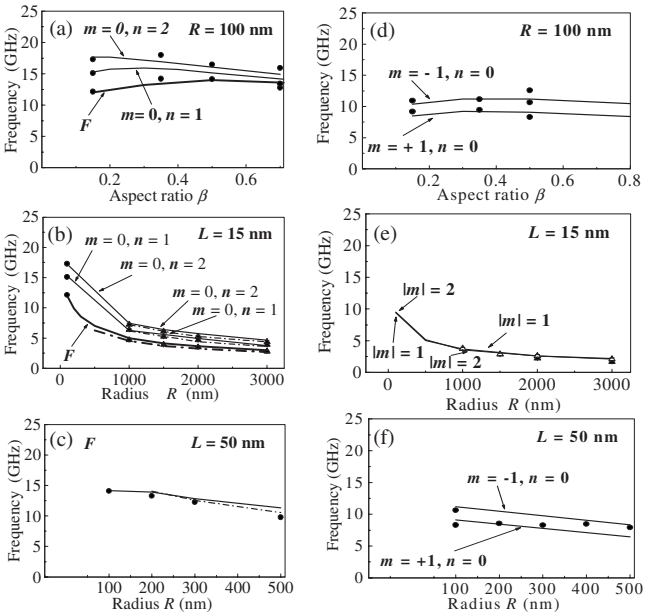

FIG. 7. Panel (a): Solid lines: frequency behavior of the most representative axially symmetric modes for radius $R=100$ nm vs β according to Eq. (16a) for nonuniform magnetization along z. Full circles: BLS data from Ref. 8. Panel (b): Solid lines: as in panel (a) but as a function of R for $L=15$ nm and for uniform magnetization. Dashed-dotted lines: the frequencies are obtained according to Eq. (16a) for uniform magnetization along the thickness by using the trial radial eigenfunction $J_1(\kappa_n \rho)$ for $n=0,1,2$. Full circles: BLS data from Ref. 8. Full up-triangles: TRKM data from Ref. 11. Panel (c): Solid line: frequencies of the F mode as a function of R for $L=50$ nm according to Eq. (16a) for nonuniform magnetization along z. Dashed line: the frequencies are obtained according to Eq. (16a) for uniform magnetization along z by using the trial radial eigenfunction $J_1(\kappa_0 \rho)$. Full circles: BLS data (the BLS data are courtesy of Gubbiotti and Carlotti, Perugia). The bold lines in panels (a) and (b) mark the calculated mode frequency (F) associated with the predominant spectral line. Panel (d): as in panel (a) but for the $m=\pm 1$ and $n=0$ modes. The meaning of the symbols is the same as in panel (a) (from Ref. 8). Panel (e): frequency behavior of the $|m|=1$ and $n=0$ and of the $|m|=2$ and $n=0$ modes vs R. Solid line: calculated frequencies by means of Eq. (16a) for uniform magnetization along the thickness. Open up triangles: TRKM measured frequencies of the $m=1$ and $n=0$ modes (in Ref. 11). Full up triangles: TRKM measured frequencies of the $m=2$ and $n=0$ modes (from Ref. 11). Panel (f): as in panel (c) but for the $m=\pm 1$ and $n=0$ modes. The meaning of the symbols is the same as in panel (c). The BLS data are courtesy of Gubbiotti and Carlotti, Perugia.

2. Comparison with experimental data

In Fig. 7 the calculated frequencies of the modes that are more active in the scattering cross section are compared with experimental data. Panel (a) displays this comparison as a function of the aspect ratio β at a fixed radius $R=100$ nm. The frequencies obtained by means of Brillouin light scattering (BLS) were measured from arrays of dots whose interdot

separation is equal to $2R$ so that the interdot dipolar coupling can be considered negligible. The good fit between calculated and measured frequencies allows us to identify unambiguously the different modes as a function of the radial number. The overall agreement with BLS data[8] is very good at small β. Instead, at large β the F mode calculated frequencies seem to overestimate the experimental frequencies. For $\beta=0.80$ this overestimation is of the order of 5%. This disagreement may be ascribed to some of the assumptions made within the present model. In particular, it may be due to the fact that the twisting effect of the static magnetization in dots of moderate aspect ratios[9] has not been taken into account in this model. This approximation can affect the calculation of both the static and dynamic contributions appearing in the quantized spectrum [cf. Eq. (16a)]. Furthermore, the diagonal approximation for the calculation of the quantized spectrum could be a further source of error for the estimation of the frequencies for any β. Finally, the $m=0$ and $n=2$ mode frequencies underestimate the BLS frequencies especially at $\beta=0.35$ and at $\beta=0.80$. Notice that in the calculation of the corresponding dipolar matrix elements we have assumed that the scattering amplitude σ_{02} is negligible likewise σ_{01}.

The agreement between theory and experiment is very good both in the nanometric and in the micrometric scale for the frequencies of the F, $m=0$ and $n=1$, and $m=0$ and $n=2$ modes, respectively, versus R [panel (b)]. The calculation of the $m=0$, $n=1$ and $m=0$, $n=2$ mode frequencies is less detailed for R in the submicrometric range with respect to the one of the F mode because, differently from the F mode, we were mainly interested in comparing the theoretical frequencies with measurements available for dots of $R \geq 1000$ nm. In the submicrometric and in the micrometric range the dash-dotted lines ($R \geq 500$ nm for F, $R \geq 1000$ nm for $m=0$, $n=1$, and $m=0$, $n=2$ modes, respectively) represent the frequencies calculated by using as trial radial eigenfunction the Bessel function of the first kind $J_1(\kappa_n \rho)$ with $n=0,1,2$. One sees that the agreement of these calculated frequencies with TRKM data is excellent. The slight downshift with respect to the frequencies obtained using as the radial eigenfunction a form proportional to $J_0(\kappa_{0n})+\sigma_{0n}Y_0(\kappa_{0n})$ is due to the smaller values of the corresponding dipolar matrix elements. Similar conclusions can be drawn from the analysis of the results reported in panel (c) for thicker dots of $L=50$ nm. In this case the comparison with the measured BLS data is performed for the calculated F mode frequencies only and for radii ranging between $R=100$ nm and $R=500$ nm where BLS data are available.

In panel (d) the $m=\pm 1$ and $n=0$ frequencies obtained according to Eq. (16a) under the assumption of nonuniform magnetization along z are displayed. The agreement with the BLS frequencies is very good for $\beta=0.50$. For smaller β the calculated frequencies are slightly downshifted with respect to the measured frequencies, and this discrepancy is more evident for $\beta=0.15$. We believe that the BLS frequency at $\beta=0.50$ nm at 12.6 GHz may be assigned to a spin excitation localized within a transition zone surrounding the vortex core as supported by the micromagnetic results of Ref. 9. Also for the comparisons shown in panels (c) and (d) the good fit between experiment and theory allows us to identify unambiguously the discussed spin modes.

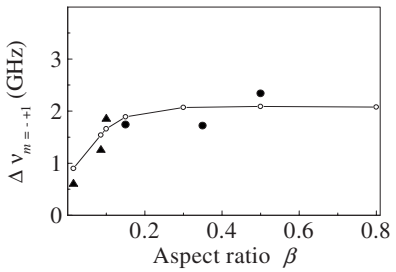

FIG. 8. Frequency splitting of the $m=\pm 1$ modes vs β. Open circles: calculated splitting. The line connecting the points is a guide to the eye. Full circles: BLS data from Ref. 8. Full up-triangles: TRKM data from Refs. 5, 7, and 14.

In panel (e) we show the mean frequencies labeled with $|m|=1$ and $|m|=2$ of the $m=\pm 1$, $n=0$ and $m=\pm 2$, $n=0$ doublets, respectively, compared to the TRKM frequencies measured applying a magnetic tipping pulse field perpendicular to the dot plane.[11] This procedure is only approximately true for the $m=\pm 1$ and $n=0$ doublets whose corresponding scattering amplitudes $\sigma_{\pm 10}$ do not have exactly opposite values. However, we have found that the dipolar matrix elements $d_{\rho\rho}^{10}$ and d_{zz}^{10}, calculated by using it as radial eigenfunction (a form proportional to the $J_1(\kappa_{10}\rho)$ Bessel function of the first kind only), are very close to the mean values of the corresponding $d_{\rho\rho}^{\pm 10}$ and $d_{zz}^{\pm 10}$ matrix elements, respectively. The overall agreement between theory and experiment is excellent for the $|m|=1$ frequencies and is very good for the $|m|=2$ frequencies. The slight overestimation of the $m=2$ and $n=0$ TRKM frequencies at large radii may be due to the choice of the $J_2(\kappa_{\pm 20}\rho)$ radial part of the trial eigenfunction instead of $J_1(\kappa_0\rho)$ that should be more plausible in the micrometric range.

The calculated frequencies of the $m=\pm 1$ and $n=0$ modes according to Eq. (16a) as a function of R for $L=50$ nm are compared with the BLS data [panel (f)]. As expected, the gap between the two frequency curves reduces with increasing R, but also at $R=500$ nm, is larger than 1 GHz. The full circles correspond to well-resolved peaks of BLS spectra at different R for this range of frequencies, but a calculation of the scattering cross section for $R>100$ nm would be required to confirm that the BLS peaks are those corresponding to the $m=\pm 1$ and $n=0$ doublets. Finally, notice that, in spite of good estimation of the corresponding measured splitting (see Fig. 8), the calculated frequencies for $R \geq 500$ nm overestimate by more than 1 GHz the experimental frequencies of the $m=\pm 1$ doublet measured with the TRKM technique[6] and not shown here.

Figure 8 shows the comparison of the calculated frequency splitting of the $m \pm 1$ and $n=0$ modes with the experiment. Different from recent analytical models, which largely underestimate the splitting of this doublet,[1,13] our calculations are in very good agreement with measurements. The frequency splitting monotonically increases with increasing β, and the rate of increase becomes lower at large aspect ratios. The measured splitting at $\beta=0.086$ and at $\beta=0.10$ and for radii in the submicrometric range have been obtained with the TRKM technique reported in Refs. 5 and 6, respectively. Instead the measured splitting shown at β

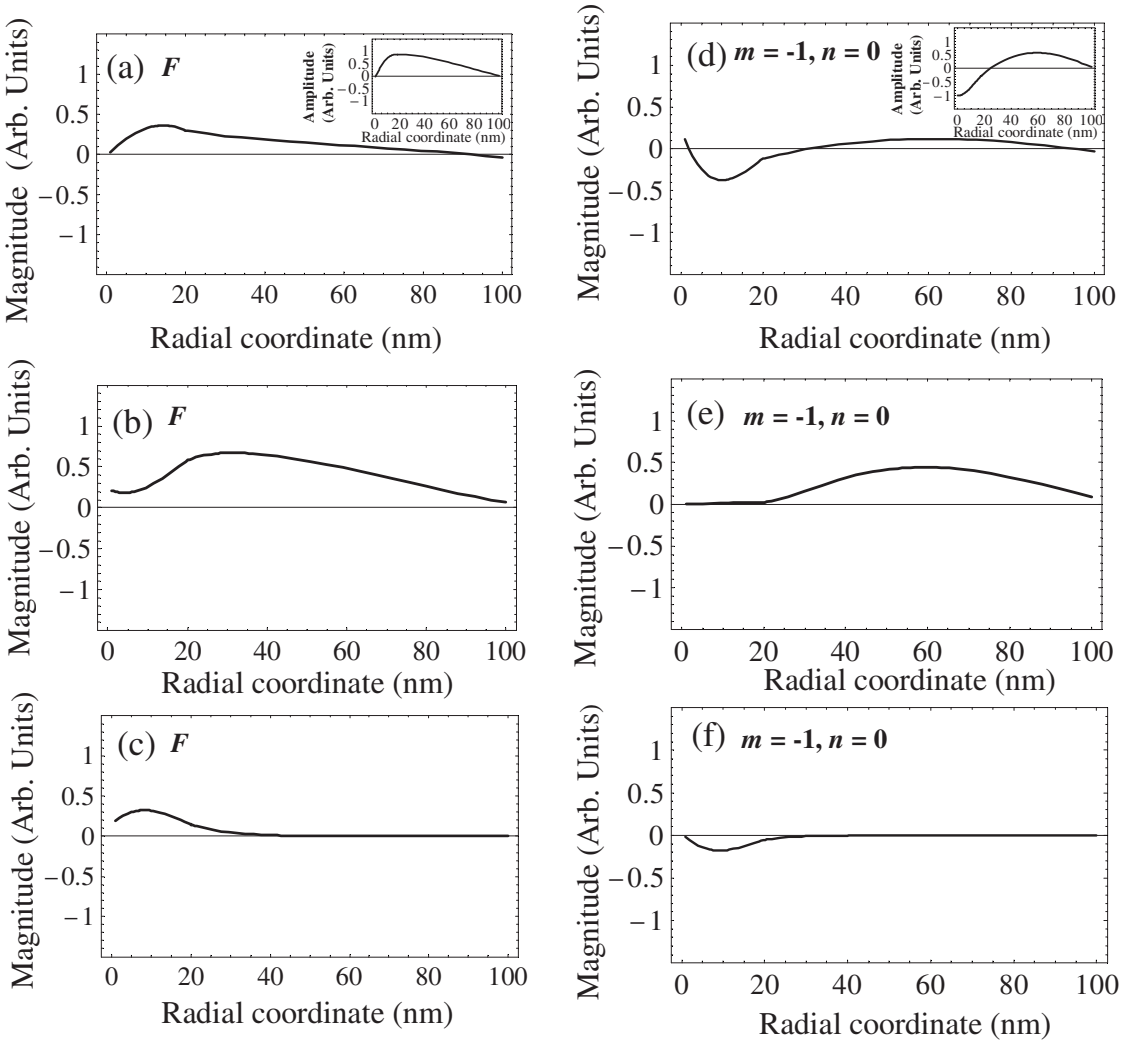

FIG. 9. Panel (a): radial profile of the $h_d^{\rho 00}$ component in a dot of radius $R=100$ nm and thickness $L=15$ nm. Inset: radial profile of the corresponding m_ρ^{00} component. Panel (b): as in panel (a) but for $h_d^{z\mathrm{OC}00}$. Panel (c): as in panel (a) but for $h_d^{z\mathrm{C}00}$. Panel (d): radial profile of $h_d^{\rho -10}$ in a dot of radius $R=100$ nm and thickness $L=15$ nm. Inset: radial profile of the corresponding m_ρ^{-10} component. Panel (e): as in panel (d) but for the $h_d^{z\mathrm{OC}-10}$ component. Panel (f): as in panel (d) but for the $h_d^{z\mathrm{C}-10}$ component. The components m_ρ, h_d^ρ, and h_d^z were plotted for each mode apart from the corresponding complex magnetization amplitudes.

$=0.015$ has been obtained with the TRKM technique but for dots of radius in the micrometric range, viz. $R=1000$ nm (Ref. 14). We show for $\beta \geq 0.15$ the frequency splitting obtained in dots of radius $R=100$ nm by the BLS spectra for different L. The slight discrepancy at small β between the calculated and the measured splitting may be due to an overestimation of the effect of C due to the approach followed for the calculation of $d_{\rho\rho}^{\pm 10}$ and $\bar{d}_{\rho\rho}^{\pm 10}$ for dots of radius in the submicrometric and micrometric range described previously.

The approximated formula of Eqs. (17a) and (17b) reproduces the exact calculation for dots with $\beta \geq 0.50$ for $R=100$ nm and for dots of radius $R>200$ nm for any β where the static exchange effects are negligible. We have found that the dynamic dipolar term of Eq. (17b) for a typical radius $R=100$ nm and for the whole range of thicknesses investigated gives a contribution of about 80% to the frequency splitting, while the mixed dipole-exchange and the nonuniform dynamic-exchange terms contribute for the remaining 20%. For larger radii the source of frequency splitting is of purely dipolar origin.

3. Spatial profiles of the most representative spin modes

The radial profiles of the dynamic dipolar magnetic field (ρ and z components) of the F mode in a thin dot are shown in Fig. 9 [panels (a)–(c)]. These profiles have been obtained according to Eqs. (7) and (8). In particular, the analytical integration over k has been followed by the numerical integration over ρ' for different values of ρ. Then an interpolation procedure has been performed. Panel (a) displays the $h_{d\rho}^{00}(\rho)$ component. Its radial profile is very similar to that of the corresponding $m_\rho^{00}(\rho)$ component shown in the inset whose profile is mainly localized in the OC region of the dot. However, the different degree of pinning on the dot border of the dynamic dipolar magnetic field is the evidence of its nonlocal character. In panel (b) one sees that the $h_{dz}^{\mathrm{OC}00}(\rho)$ component is mainly localized in the OC region even though

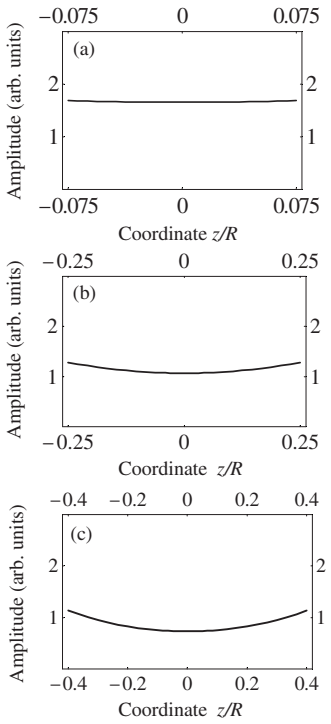

FIG. 10. Panel (a): z profile of m_{ρ}^{00} for the F mode in a dot of radius $R=100$ nm and thickness $L=15$ nm. $z/R=-0.075$ corresponds to the lower endface surface and $z/R=0.075$ corresponds to the upper endface surface. Panel (b): as in panel (a) but for $L=50$ nm. Panel (c): as in panel (a) but for $L=80$ nm. The component m_{00}^{ρ} was plotted apart from the corresponding complex magnetization amplitude.

its profile has a tail in the C region. Instead, $h_{dz}^{C00}(\rho)$ has an almost vanishing magnitude in the dot center, is mainly localized in the C region, and progressively decays going toward the dot border as depicted in panel (c). This behavior indicates that, due to their nonlocal character, both the C and OC dynamic dipolar magnetic fields are not strictly localized in the C and OC regions, respectively.

The corresponding radial profiles of the dynamic dipolar components of the $m=-1$ and $n=0$ mode $[h_{d\rho}^{-10}(\rho,\phi)$, $h_{dz}^{OC-10}(\rho,\phi)$, and $h_{dz}^{C-10}(\rho,\phi)$, respectively] have been calculated according to Eqs. (11), (12a), and (12b) with the same calculation procedure used for the F mode and are summarized in panels (d)–(f). In panel (d) the radial profile of $h_{d\rho}^{-10}(\rho,\phi)$ is shown. Because of its nonlocal character, the degree of pinning at the dot center is much more important with respect to the one of the radial profile of the $m_{\rho}^{-10}(\rho,\phi)$ component [inset to panel (d)], which is instead almost unpinned. At the dot border both profiles are strongly pinned but with a slightly different degree of pinning. The radial profiles of the $h_{dz}^{OC-10}(\rho,\phi)$ and $h_{dz}^{C-10}(\rho,\phi)$ components may be understood by means of the same arguments presented for the F mode. Also in this case the effect of the nonlocal character of the dynamic dipolar magnetic field is highlighted. Similar considerations can be carried on for the dynamic dipolar magnetic field profile of the $m=+1$ and $n=0$ modes not reported here.

In Fig. 10 some profiles along z for a dot of radius $R=100$ nm and for different thicknesses are shown. Panels (a)–(c) show the profiles along the z coordinate of the m_{ρ} component of the F mode for $L=15$ nm, $L=50$ nm, and $L=80$ nm, respectively. These z profiles have been obtained by use of a linear combination of the dynamic magnetization component m_{ρ} of one mode on the upper endface and of another mode on the lower endface, which interact with each other, taking into account that $\kappa_{\perp}^{00}=\pm i\kappa_{00}$. This combination is proportional to $[e^{-\kappa_{00}(L/2+z)}+e^{-\kappa_{00}(L/2-z)}]$ with $\kappa_{00}=(2.5\times10^5)$ cm^{-1}. As expected, one sees that the profile nonuniformity along z increases with increasing the thickness L. Similar profiles characterize the other modes. In particular, with increasing the mode number (both m and n), the disuniformity becomes more important. If one adds the wave number quantization obtained from the "mixed" exchange boundary condition along the dot thickness, the resulting effect is a more noticeable nonuniformity of the z profiles, especially in the C region. However, this further effect does not affect the spin mode frequencies. We stress that, if one would take into account the "mixed" exchange boundary condition along z only, the profile of each mode along the thickness would exhibit more or less the same degree of disuniformity, but the downshift on the spin mode frequencies would be of the same orders of magnitude of the one found according to this model. The "mixed" exchange boundary condition plays instead a crucial role for the behavior of C modes with nodes exhibiting important localization effects along the thickness. These modes found by means of micromagnetic calculations and classified as first-order (V_1) and second-order (V_2) gyrotropic vortex modes by Yan *et al.*[21] in Py rectangular prisms will be the subject of another study.

VI. CONCLUSIONS

In this paper we have studied the role of the dipolar magnetic fields on the spin mode frequencies in dots with R ranging from the nanometric to the micrometric size. The dipolar matrix elements have been calculated exactly for each spin mode examined, and the effect on the frequencies has been investigated. The general conclusion is that, aside from a few cases related to the special behavior of the inverse dynamical susceptibility fitted function, the local dipolar approximation leads to an underestimation of the frequencies.

The entity of the tridimensionality effect, partially taken into account by considering a z dependence in the dynamic magnetization, has been investigated. Its effect is to cause a slight downshift of the frequencies for dots of aspect ratio $\beta\geq0.20$ with the exception of the F mode frequency where the downshift is larger. We have also predicted the deviation from $\sqrt{\beta}$ in dots of moderate aspect ratios. The experimental splitting of the $\pm|m|$ and n doublets has been explained quantitatively in terms of both dipolar and exchange contributions. Our results are fully consistent with recent experimental findings obtained by means of different techniques and the overall agreement is very good.

ACKNOWLEDGMENTS

The authors thank G. Gubbiotti and G. Carlotti for the permission to reproduce the unpublished Brillouin light scattering data. CNISM-CNR support is also acknowledged.

APPENDIX: INTEGRALS CALCULATION AND DIAGONAL MATRIX ELEMENTS

1. Uniform magnetization along the thickness

The integrals $I^m_{\rho\rho}(\rho,\rho')$ and $I^m_{zz}(\rho,\rho')$ for $m=0,\pm1,\pm2,\ldots$ for the case of uniform magnetization are analytically calculated.

a. Axially symmetric modes

$$I^0_{\rho\rho}(\rho,\rho')=\int_0^\infty dkkf(kL)J_1(k\rho)J_1(k\rho')$$

$$=\frac{1}{\rho'}\delta(\rho'-\rho)+I^0_1(\rho,\rho')+I^0_2(\rho,\rho'),$$

where $J_1(k\rho)=-J_0'(k\rho)$. Here,

$$I^0_1(\rho,\rho')=-\frac{1}{L}\int_0^\infty dkJ_1(k\rho)J_1(k\rho')$$

$$=-\frac{1}{L}\begin{cases}\dfrac{\rho'}{2\rho^2}{}_2F_1\left[\dfrac{1}{2},\dfrac{3}{2},2,\dfrac{\rho'^2}{\rho^2}\right] & \text{if } \rho'<\rho\\ \dfrac{\rho}{2\rho'^2}{}_2F_1\left[\dfrac{1}{2},\dfrac{3}{2},2,\dfrac{\rho^2}{\rho'^2}\right] & \text{if } \rho'>\rho,\end{cases} \tag{A1}$$

$$I^0_2(\rho,\rho')=\frac{1}{L}\int_0^\infty dke^{-kL}J_1(k\rho)J_1(k\rho')=\frac{1}{L}\frac{1}{\pi(\rho\rho')^{1/2}}Q_{1/2}(s). \tag{A2}$$

Instead $I^0_{zz}(\rho,\rho')=\frac{1}{\rho'}\delta(\rho'-\rho)-\int_0^\infty dkkf(kL)J_0(k\rho)J_0(k\rho')=I^0_3(\rho,\rho')+I^0_4(\rho,\rho')$, with

$$I^0_3(\rho,\rho')=\frac{1}{L}\int_0^\infty dkJ_0(k\rho)J_0(k\rho')$$

$$=\frac{1}{L}\begin{cases}\dfrac{2}{\pi\rho}K\left[\dfrac{\rho'^2}{\rho^2}\right] & \text{if } \rho'<\rho\\ \dfrac{2}{\pi\rho'}K\left[\dfrac{\rho^2}{\rho'^2}\right] & \text{if } \rho'>\rho,\end{cases} \tag{A3}$$

$$I^0_4(\rho,\rho')=-\frac{1}{L}\int_0^\infty dke^{-kL}J_0(k\rho)J_0(k\rho')$$

$$=-\frac{1}{L}\frac{1}{\pi(\rho\rho')^{1/2}}Q_{-1/2}(s). \tag{A4}$$

These integrals are calculated after inserting $f(kL)=1-\frac{1-e^{-kL}}{kL}$. ${}_2F_1$ is the hypergeometric function, K is the complete elliptic integral of the first kind, and $Q_{1/2}$ and $Q_{-1/2}$ are Legendre functions of the second kind of fractional order $\frac{1}{2}$ and $-\frac{1}{2}$, respectively, with $s=\frac{\rho^2+\rho'^2+L^2}{2\rho\rho'}$.

b. Nonaxially symmetric modes

We write

$$\bar{I}^m_{\rho\rho}(\rho,\rho',\phi)=I^m_{\rho\rho}(\rho,\rho')e^{im\phi}$$

with

$$I^m_{\rho\rho}(\rho,\rho')=\int_0^\infty dkkf(kL)\left[J_{m-1}(k\rho)-\tfrac{m}{k\rho}J_m(k\rho)\right]\left[J_{m-1}(k\rho')-\tfrac{m}{k\rho'}J_m(k\rho')\right]=I^m_1(\rho,\rho')+I^m_6(\rho,\rho')+I^m_7(\rho,\rho')$$

after inserting $f(kL)=1-\frac{1-e^{-kL}}{kL}$ and using the Bessel recurrence relation $J'_m(x)=J_{m-1}(x)-\frac{m}{x}J_m(x)$. In particular, $I^m_6(\rho,\rho')=I^m_{6a}(\rho,\rho')+I^m_{6b}(\rho,\rho')+I^m_{6c}(\rho,\rho')+I^m_{6d}(\rho,\rho')$ and $I^m_7(\rho,\rho')=I^m_{7a}(\rho,\rho')+I^m_{7b}(\rho,\rho')+I^m_{7c}(\rho,\rho')+I^m_{7d}(\rho,\rho')$. We get

$$I^m_1(\rho,\rho')=\int_0^\infty dkk\left[J_{m-1}(k\rho)-\frac{m}{k\rho}J_m(k\rho)\right]\left[J_{m-1}(k\rho')-\frac{m}{k\rho'}J_m(k\rho')\right]=\begin{cases}\dfrac{1}{\rho'}\delta(\rho'-\rho)-\dfrac{1}{2}m\dfrac{\rho'^{(m-1)}}{\rho^{(m+1)}} & \text{if } \rho'<\rho \text{ and } m>\dfrac{1}{2}\\ \dfrac{1}{\rho'}\delta(\rho'-\rho)-\dfrac{1}{2}m\dfrac{1}{\rho^2} & \text{if } \rho'=\rho \text{ and } m>\dfrac{1}{2}\\ \dfrac{1}{\rho'}\delta(\rho'-\rho)-\dfrac{1}{2}m\dfrac{\rho^{(m-1)}}{\rho'^{(m+1)}} & \text{if } \rho'>\rho \text{ and } m>\dfrac{1}{2},\end{cases} \tag{A5}$$

$$I_{6a}^{m}(\rho,\rho') = -\frac{1}{L}\int_0^\infty dk J_{m-1}(k\rho)J_{m-1}(k\rho') = -\frac{1}{L}\begin{cases} \dfrac{1}{\pi^{1/2}}\dfrac{\Gamma\left[m-\dfrac{1}{2}\right]}{\Gamma[m]}\dfrac{\rho'^{(m-1)}}{\rho^m}{}_2F_1\left[\dfrac{1}{2},m-\dfrac{1}{2},m,\dfrac{\rho'^2}{\rho'^2}\right] & \text{if } \rho'<\rho \text{ and } m>\dfrac{1}{2} \\ \dfrac{1}{\pi^{1/2}}\dfrac{\Gamma\left[m-\dfrac{1}{2}\right]}{\Gamma[m]}\dfrac{\rho^{(m-1)}}{\rho'^m}{}_2F_1\left[\dfrac{1}{2},m-\dfrac{1}{2},m,\dfrac{\rho^2}{\rho'^2}\right] & \text{if } \rho'>\rho \text{ and } m>\dfrac{1}{2}, \end{cases} \tag{A6}$$

$$I_{6b}^{m}(\rho,\rho') = \frac{1}{L}\frac{m}{\rho}\int_0^\infty dk\frac{1}{k}J_m(k\rho)J_{m-1}(k\rho') = \frac{1}{L}\begin{cases} \dfrac{1}{\pi^{1/2}}\dfrac{\Gamma\left[m-\dfrac{1}{2}\right]}{\Gamma[m]}m\dfrac{\rho'^{(m-1)}}{\rho^m}{}_2F_1\left[-\dfrac{1}{2},m-\dfrac{1}{2},m,\dfrac{\rho'^2}{\rho^2}\right] & \text{if } \rho'<\rho \text{ and } m>\dfrac{1}{2} \\ \dfrac{1}{2(\pi)^{1/2}}\dfrac{\Gamma\left[m-\dfrac{1}{2}\right]}{\Gamma[m+1]}m\dfrac{\rho^{(m-1)}}{\rho'^m}{}_2F_1\left[\dfrac{1}{2},m-\dfrac{1}{2},m+1,\dfrac{\rho^2}{\rho'^2}\right] & \text{if } \rho'>\rho \text{ and } m>\dfrac{1}{2}, \end{cases} \tag{A7}$$

$$\begin{aligned} I_{6c}^{m}(\rho,\rho') &= \frac{1}{L}\frac{m}{\rho'}\int_0^\infty dk\frac{1}{k}J_{m-1}(k\rho)J_m(k\rho') \\ &= \frac{1}{L}\begin{cases} \dfrac{1}{2(\pi)^{1/2}}\dfrac{\Gamma\left[m-\dfrac{1}{2}\right]}{\Gamma[m+1]}m\dfrac{\rho'^{(m-1)}}{\rho^m}{}_2F_1\left[\dfrac{1}{2},m-\dfrac{1}{2},m+1,\dfrac{\rho'^2}{\rho^2}\right] & \text{if } \rho'<\rho \text{ and } m>\dfrac{1}{2} \\ \dfrac{1}{\pi^{1/2}}\dfrac{\Gamma\left[m-\dfrac{1}{2}\right]}{\Gamma[m]}m\dfrac{\rho^{(m-1)}}{\rho'^m}{}_2F_1\left[-\dfrac{1}{2},m-\dfrac{1}{2},m,\dfrac{\rho^2}{\rho'^2}\right] & \text{if } \rho'>\rho \text{ and } m>\dfrac{1}{2}, \end{cases} \end{aligned} \tag{A8}$$

$$\begin{aligned} I_{6d}^{m}(\rho,\rho') &= -\frac{1}{L}\frac{m^2}{\rho\rho'}\int_0^\infty dk\frac{1}{k^2}J_m(k\rho)J_m(k\rho') = \\ &-\frac{1}{L}\begin{cases} \dfrac{1}{2(\pi)^{1/2}}\dfrac{\Gamma\left[m-\dfrac{1}{2}\right]}{\Gamma[m+1]}m^2\dfrac{\rho'^{(m-1)}}{\rho^m}{}_2F_1\left[-\dfrac{1}{2},m-\dfrac{1}{2},m+1,\dfrac{\rho'^2}{\rho^2}\right] & \text{if } \rho'<\rho \text{ and } m>\dfrac{1}{2} \\ \dfrac{1}{2(\pi)^{1/2}}\dfrac{\Gamma\left[m-\dfrac{1}{2}\right]}{\Gamma[m+1]}m^2\dfrac{\rho^{(m-1)}}{\rho'^m}{}_2F_1\left[-\dfrac{1}{2},m-\dfrac{1}{2},m+1,\dfrac{\rho^2}{\rho'^2}\right] & \text{if } \rho'>\rho \text{ and } m>\dfrac{1}{2}. \end{cases} \end{aligned} \tag{A9}$$

$\Gamma[x]$ is the Euler function of argument x,

$$I_{7a}^{m}(\rho,\rho') = \frac{1}{L}\int_0^\infty dk e^{-kL}J_{m-1}(k\rho)J_{m-1}(k\rho') = \frac{1}{L}\frac{1}{\pi(\rho\rho')^{1/2}}Q_{m-3/2}(s), \tag{A10}$$

with $Q_{m-3/2}$ the Legendre function of the second kind of fractional order. It is[26]

$$\begin{aligned} I_{7b}^{m}(\rho,\rho') &= -\frac{1}{L}\frac{1}{2}\frac{m}{\rho}\int_0^\infty dk\frac{1}{k}e^{-kL}J_m(k\rho)J_{m-1}(k\rho') \\ &= -\frac{1}{L}\frac{1}{2}\frac{m}{\rho}\frac{\Gamma[2m-1]\left(\dfrac{1}{2}\rho'\right)^{m-1}\left(\dfrac{1}{2}\rho\right)^m}{\Gamma\left[\dfrac{1}{2}\right]\Gamma\left[m+\dfrac{1}{2}\right]}\int_0^\pi d\tilde{\varphi}\frac{\sin^{2m}\tilde{\varphi}}{(L^2+2iL\rho\cos\tilde{\varphi}-\rho^2\cos^2\tilde{\varphi}+\rho'^2)^{m-1/2}}. \end{aligned} \tag{A11}$$

$I_{7c}^{m}(\rho,\rho')$ is obtained from $I_{7b}^{m}(\rho,\rho')$ by interchanging ρ with ρ'. The integral on the second member of Eq. (A11) may be solved analytically, and $I_{7b}^{m}(\rho,\rho')$ is expressed in terms of elliptic integrals of the first kind $F[\varphi,k]$, elliptic integrals of the second kind $E[\phi,\bar{k}]$ and $E[\frac{1}{\varphi},\frac{1}{\bar{k}}]$, and incomplete elliptic integrals of the third kind $\Pi[\bar{n},\phi,\bar{k}]$. φ, k, $\bar{k}$, ϕ, $\frac{1}{\varphi}$, $\frac{1}{\bar{k}}$, and $\bar{n}$ are different arguments of the complete elliptic integrals. A similar expression may be found for $I_{7c}^{m}(\rho,\rho')$. Using the Bessel recurrence relation $J_m(x)=\frac{x}{2m}[J_{m+1}(x)+J_{m-1}(x)]$ the integral I_{7d} instead may be written as

$$I_{7d}^{m}(\rho,\rho')=\frac{1}{L}\frac{1}{4}\left[\int_0^\infty dke^{-kL}J_{m+1}(k\rho)J_{m+1}(k\rho')-\int_0^\infty dke^{-kL}J_{m-1}(k\rho)J_{m-1}(k\rho')\right]=\frac{1}{L}\frac{1}{4}\frac{1}{\pi(\rho\rho')^{1/2}}[Q_{m+1/2}(s)-Q_{m-3/2}(s)], \tag{A12}$$

with $Q_{m+1/2}$ and $Q_{m-3/2}$ the Legendre functions of fractional order.

Instead $\bar{I}_{zz}^{m}(\rho,\rho',\phi)=I_{zz}^{m}(\rho,\rho')e^{im\phi}$, with $I_{zz}^{m}(\rho,\rho')=\frac{1}{\rho'}\delta(\rho'-\rho)-\int_0^\infty dkkf(kL)J_m(k\rho)J_m(k\rho')=I_8^m(\rho,\rho')+I_9^m(\rho,\rho')$, where

$$I_8^m(\rho,\rho')=\frac{1}{L}\int_0^\infty dkJ_m(k\rho)J_m(k\rho')=\frac{1}{L}\begin{cases}\dfrac{1}{\pi^{1/2}}\dfrac{\Gamma\left[m+\frac{1}{2}\right]}{\Gamma[m+1]}\dfrac{\rho'^m}{\rho^{(m+1)}}{}_2F_1\left[\dfrac{1}{2},m+\dfrac{1}{2},m+1,\dfrac{\rho'^2}{\rho^2}\right] & \text{if } \rho'<\rho \\ \dfrac{1}{\pi^{1/2}}\dfrac{\Gamma\left[m+\frac{1}{2}\right]}{\Gamma[m+1]}\dfrac{\rho^m}{\rho'^{(m+1)}}{}_2F_1\left[\dfrac{1}{2},m+\dfrac{1}{2},m+1,\dfrac{\rho^2}{\rho'^2}\right] & \text{if } \rho'>\rho,\end{cases} \tag{A13}$$

$$I_9^m(\rho,\rho')=-\frac{1}{L}\int_0^\infty dke^{-kL}J_m(k\rho)J_m(k\rho')=-\frac{1}{L}\frac{1}{\pi(\rho\rho')^{1/2}}Q_{m-1/2}(s), \tag{A14}$$

using $f(kL)=1-\frac{1-e^{-kL}}{kL}$.

c. Diagonal matrix elements

The OC and C diagonal dipolar matrix elements of Eq. (16a) read as

$$d_{ii}^{Xmn}=\frac{\int d^2\boldsymbol{\rho}m_i^{*mn}(\boldsymbol{\rho})h_{di}^{Xmn}(\boldsymbol{\rho})}{4\pi N_{ii}^{mn}}, \tag{A15}$$

with $X=\mathrm{OC},\mathrm{C}$ and $d_{ii}^{mn}=d_{ii}^{\mathrm{OC}mn}+d_{ii}^{\mathrm{C}mn}$ with $i=\rho,z$. The integration is carried out over the dot area and $N_{ii}^{mn}=\int d^2\boldsymbol{\rho}m_i^{*mn}(\boldsymbol{\rho})m_i^{mn}(\boldsymbol{\rho})$ is the in-plane part of the normalization constant (integral) of the m_i component of the dynamic magnetization. We have neglected the sin θ dependence of $m_\rho^{*mn}(\boldsymbol{\rho})$ in the C region, because in Eq. (2) the two dynamic magnetization components m_ρ and m_z of the OC region appear. By using $h_{d\rho}^{\mathrm{OC}0n}$ and $h_{d\rho}^{\mathrm{C}0n}$ for $m=0$, n modes [cf. Eq. (10)] together with the corresponding $h_{d\rho}^{\mathrm{OC}mn}$ and $h_{d\rho}^{\mathrm{C}mn}$ [cf. Eqs. (14a) and (14b)] for $|m|\neq 0$, n modes, respectively, written within the local dipolar approximation we get $d_{\rho\rho}^{mn}\simeq -f(\beta\alpha_{mn})\mathrm{C}_{mn}$. For $m=0$, n modes we get $\mathrm{C}_{0n}=1$ for each n, while for $|m|\neq 0$ and n modes, we obtain

$$\mathrm{C}_{mn}=\left\{\int_\epsilon^R\rho d\rho[J_{|m|}(\kappa_{mn}\rho)-\sigma_{mn}Y_{|m|}(\kappa_{mn}\rho)]Q\times\int_0^\infty dkkJ'_m(k\rho)J'_m(k\rho')\right\}\Bigg/\left(\int_\epsilon^R\rho d\rho[J_{|m|}(\kappa_{mn}\rho)-\sigma_{mn}Y_{|m|}(\kappa_{mn}\rho)]^2\right), \tag{A16}$$

where $Q=\int_\epsilon^a\rho'd\rho'[J_{|m|}(\kappa_{mn}\rho')-\sigma_{mn}Y_{|m|}(\kappa_{mn}\rho')]\sin\theta(\rho')+\int_a^R\rho'd\rho'[J_{|m|}(\kappa_{mn}\rho')-\sigma_{mn}Y_{|m|}(\kappa_{mn}\rho')]$, with $m=\pm1,\pm2,\ldots$ and $n=0,1,\ldots$.

The calculation of the integral over k yields to the result given in the right member of Eq. (A5). Using Eq. (13), which expresses $h_{dz}^{\mathrm{OC}mn}$ and $h_{dz}^{\mathrm{C}mn}$ written within the local approximation yields

$$d_{zz}^{\mathrm{OC}mn}\simeq-\{(1-\eta)[1-f(\beta\alpha_{mn})]\}$$

and

$$d_{zz}^{\mathrm{C}mn}\simeq-b\eta[1-f(\beta\alpha_{mn})],$$

respectively.

2. Nonuniform magnetization along the thickness

a. Axially symmetric modes

We calculate after inserting $f(kL,\beta\alpha_{0n})$ [cf. Eq. (15) for $m=0$] in place of $f(kL)$,

$$\bar{I}^0_{\rho\rho}(\rho,\rho',\beta\alpha_{0n}) = \int_0^\infty dkkf(kL,\beta\alpha_{0n})J_1(k\rho)J_1(k\rho')$$
$$= \bar{I}^0_1(\rho,\rho')L + \{\beta\alpha_{0n}[\coth(\beta\alpha_{0n})\bar{I}^0_2(\rho,\rho') + 1/\sinh(\beta\alpha_{0n})\bar{I}^0_3(\rho,\rho')]\},$$

where

$$\bar{I}^0_j(\rho,\rho') = \frac{1}{L}\int_0^\infty dkS_j(k,\kappa_{0n})J_1(k\rho)J_1(k\rho'), \quad \text{(A17)}$$

with $j=1,2,3$, $S_1(k,\kappa_{0n})=\frac{k^3}{k^2-\kappa_{0n}^2}$, $S_2(k,\kappa_{0n})=-\frac{k^2}{k^2-\kappa_{0n}^2}$, and $S_3(k,\kappa_{0n})=e^{-kL}\frac{k^2}{k^2-\kappa_{0n}^2}$. Straightforwardly, for $\kappa_{0n}\to 0$ $\bar{I}^0_{\rho\rho}(\rho,\rho',\beta\alpha_{0n})$ reduces to $I^0_{\rho\rho}(\rho,\rho')$, the corresponding quantity of the uniform case.

Instead,

$$\bar{I}^0_{zz}(\rho,\rho',\beta\alpha_{0n}) = \frac{1}{\rho'}\delta(\rho'-\rho) - \int_0^\infty dkkf(kL,\beta\alpha_{0n})J_0(k\rho)J_0(k\rho')$$
$$= \beta\alpha_{0n}[\coth(\beta\alpha_{0n})\bar{I}^0_4(\rho,\rho') + 1/\sinh(\beta\alpha_{0n})\bar{I}^0_5(\rho,\rho')],$$

with

$$\bar{I}^0_l(\rho,\rho') = \frac{1}{L}\int_0^\infty dkS_l(k,\kappa_{0n})J_0(k\rho)J_0(k\rho'), \quad \text{(A18)}$$

where $l=4,5$, $S_4(k,\kappa_{0n})=-S_2(k,\kappa_{0n})$, and $S_5(k,\kappa_{0n})=-S_3(k,\kappa_{0n})$. Straightforwardly, for $\kappa_{0n}\to 0$ $\bar{I}^0_{zz}(\rho,\rho',\beta\alpha_{0n})$ reduces to $I^0_{zz}(\rho,\rho')$ of the uniform case.

b. Nonaxially symmetric modes

The corresponding $\bar{I}^m_{\rho\rho}$ component for $|m|\neq 0$ and n modes obtained by use of Eq. (6) is $\tilde{\bar{I}}^m_{\rho\rho}(\rho,\rho',\beta\alpha_{mn},\phi) = e^{im\phi}\bar{I}^m_{\rho\rho}(\rho,\rho',\beta\alpha_{mn})$, with

$$\bar{I}^m_{\rho\rho}(\rho,\rho',\beta\alpha_{mn}) = \int_0^\infty dkkf(kL,\beta\alpha_{mn})J'_m(k\rho)J'_m(k\rho')$$
$$= \bar{I}^m_6(\rho,\rho')L + \{\beta\alpha_{mn}[\coth(\beta\alpha_{mn})\bar{I}^m_7(\rho,\rho') + 1/\sinh(\beta\alpha_{mn})\bar{I}^m_8(\rho,\rho')]\}$$

after inserting $f(kL,\beta\alpha_{mn})$ [cf. Eq. (15) for $m\neq 0$] in place of $f(kL)$ and

$$\bar{I}^m_p(\rho,\rho') = \frac{1}{L}\int_0^\infty dkS_p(k,\kappa_{mn})J'_m(k\rho)J'_m(k\rho'), \quad \text{(A19)}$$

with $p=6,7,8$, $S_6(k,\kappa_{mn})=\frac{k^3}{k^2-\kappa_{mn}^2}$, $S_7(k,\kappa_{mn})=-\frac{k^2}{k^2-\kappa_{mn}^2}$, and $S_8(k,\kappa_{mn})=e^{-kL}\frac{k^2}{k^2-\kappa_{mn}^2}$. Again, $\tilde{\bar{I}}^m_{\rho\rho}(\rho,\rho',\kappa_{mn},\phi)$ reduces to $\bar{I}^m_{\rho\rho}(\rho,\rho',\phi)$ of the uniform case for $\kappa_{mn}\to 0$.

Instead, using Eq. (6) the $\tilde{\bar{I}}^m_{zz}(\rho,\rho',\beta\alpha_{mn},\phi)$ quantity for $m\neq 0$ and n reads $\tilde{\bar{I}}^m_{zz}(\rho,\rho',\beta\alpha_{mn},\phi) = e^{im\phi}\bar{I}^m_{zz}(\rho,\rho',\beta\alpha_{mn})$, with

$$\bar{I}^m_{zz}(\rho,\rho',\beta\alpha_{mn}) = \frac{1}{\rho'}\delta(\rho'-\rho) - \int_0^\infty dkkf(kL,\beta\alpha_{mn})J_m(k\rho)J_m(k\rho')$$
$$= \beta\alpha_{mn}[\coth(\beta\alpha_{mn})\bar{I}^m_9(\rho,\rho') + 1/\sinh(\beta\alpha_{mn})\bar{I}^m_{10}(\rho,\rho')]$$

and

$$\bar{I}^m_q(\rho,\rho') = \frac{1}{L}\int_0^\infty dkS_q(k,\kappa_{mn})J_m(k\rho)J_m(k\rho'), \quad \text{(A20)}$$

with $q=9,10$, $S_9(k,\kappa_{mn})=-S_7(k,\kappa_{mn})$, and $S_{10}(k,\kappa_{mn})=-S_8(k,\kappa_{mn})$. $\tilde{\bar{I}}^m_{zz}(\rho,\rho',\beta\alpha_{mn},\phi)$ reduces to $\bar{I}^m_{zz}(\rho,\rho',\phi)$ of the uniform case for $\kappa_{mn}\to 0$. A numerical evaluation of the integrals in Eqs. (A17) and (A18) [Eqs. (A19) and (A20)] for each κ_{0n} (κ_{mn}) has been carried out very carefully excluding the singularities at $k=\kappa_{0n}$ ($k=\kappa_{mn}$) for each n.

c. Diagonal matrix elements

The OC and C dipolar diagonal matrix elements are written as

$$\bar{d}^{Xmn}_{ii} = \frac{\int d^3\mathbf{r}m_i^{*mn}(\mathbf{r})h^{Xmn}_{di}(\mathbf{r})}{4\pi\bar{N}^{mn}_{ii}}, \quad \text{(A21)}$$

with $X=\mathrm{OC},\mathrm{C}$. Here $\bar{N}^{mn}_{ii}=\int d^3\mathbf{r}m_i^{*mn}(\mathbf{r})m_i^{mn}(\mathbf{r}) = \int dzm_i^{*mn}(z)m_i^{mn}(z)\times\int d^2\boldsymbol{\rho}m_\rho^{*mn}(\boldsymbol{\rho})m_\rho^{mn}(\boldsymbol{\rho})$ is the normalization constant (integral) of the m_i component of the dynamic magnetization with $i=\rho,z$. We get for the whole set of modes $\bar{d}_{\rho\rho}\simeq-\chi(\beta\alpha_{mn})\mathrm{C}_{mn}$ (or $\bar{d}_{\rho\rho}\simeq-\chi_f(\beta\alpha_{mn})\mathrm{C}_{mn}$). Such as for the case of uniform magnetization along z the calculated coefficients C_{mn} are those given in Eq. (A16) for $|m|$ and n modes; in particular, $\mathrm{C}_{mn}=1$ for $m=0$ and n modes. By using the expressions of the z components of the dipolar magnetic fields derived within the local dipolar approximation for $m=0$ and n modes and for $|m|\neq 0$ and n modes, we get $\bar{d}^{\mathrm{OC}mn}_{zz}\simeq-\{(1-\eta)[1-\chi(\beta\alpha_{mn})]\}$ {or $\bar{d}^{\mathrm{OC}mn}_{zz}\simeq-\{(1-\eta)[1-\chi_f(\beta\alpha_{mn})]\}$} and $\bar{d}^{\mathrm{C}mn}_{zz}\simeq-b\eta[1-\chi(\beta\alpha_{mn})]$ {or $\bar{d}^{\mathrm{C}mn}_{zz}\simeq-b\eta[1-\chi_f(\beta\alpha_{mn})]$}, respectively.

[1] B. A. Ivanov and C. E. Zaspel, Appl. Phys. Lett. **81**, 1261 (2002).
[2] K. Y. Guslienko, B. A. Ivanov, V. Novosad, Y. Otani, H. Shinia, and K. Fukamichi, J. Appl. Phys. **91**, 8037 (2002).
[3] V. Novosad, K. Y. Guslienko, H. Shima, Y. Otani, S. G. Kim, K. Fukamichi, N. Kikuchi, O. Kitakami, and Y. Shimada, Phys. Rev. B **65**, 060402(R) (2002).
[4] M. Buess, R. Höllinger, T. Haug, K. Perzlmaier, U. Krey, D. Pescia, M. R. Scheinfein, D. Weiss, and C. H. Back, Phys. Rev. Lett. **93**, 077207 (2004).
[5] X. Zhu, Z. Liu, V. Metlushko, P. Grütter, and M. Freeman, Phys. Rev. B **71**, 180408(R) (2005).
[6] J. P. Park and P. A. Crowell, Phys. Rev. Lett. **95**, 167201 (2005).
[7] C. E. Zaspel, B. A. Ivanov, J. P. Park, and P. A. Crowell, Phys. Rev. B **72**, 024427 (2005).
[8] F. Montoncello and F. Nizzoli, in *Magnetic Properties of Laterally Confined Nanometric Structures*, edited by G. Gubbiotti (Transworld Research Network, Kerala, India, 2006).
[9] F. Boust and N. Vukadinovic, Phys. Rev. B **70**, 172408 (2004).
[10] M. Buess, Y. Acremann, A. Kashuba, C. H. Back, and D. Pescia, J. Phys.: Condens. Matter **15**, R1093 (2003).
[11] M. Buess, T. P. J. Knowles, R. Höllinger, T. Haug, U. Krey, D. Weiss, D. Pescia, M. R. Scheinfein, and C. H. Back, Phys. Rev. B **71**, 104415 (2005).
[12] B. A. Ivanov and C. E. Zaspel, Phys. Rev. Lett. **94**, 027205 (2005).
[13] R. Zivieri and F. Nizzoli, Phys. Rev. B **71**, 014411 (2005), and references cited therein; R. Zivieri and F. Nizzoli, *ibid.* **74**, 219901(E) (2006).
[14] F. Hoffmann, G. Woltersdorf, K. Perzlmaier, A. N. Slavin, V. S. Tiberkevich, A. Bischof, D. Weiss, and C. H. Back, Phys. Rev. B **76**, 014416 (2007).
[15] N. A. Usov and S. E. Peschany, J. Magn. Magn. Mater. **118**, L290 (1993).
[16] E. Feldtkeller and H. Thomas, Phys. Kondens. Mater. **4**, 8 (1965).
[17] R. Zivieri and R. L. Stamps, Phys. Rev. B **73**, 144422 (2006).
[18] R. W. Damon and J. R. Eshbach, J. Phys. Chem. Solids **19**, 308 (1961).
[19] K. Y. Guslienko, W. Scholz, R. W. Chantrell, and V. Novosad, Phys. Rev. B **71**, 144407 (2005).
[20] K. Yu. Guslienko, S. O. Demokritov, B. Hillebrands, and A. N. Slavin, Phys. Rev. B **66**, 132402 (2002).
[21] M. Yan, R. Hertel, and C. M. Schneider, Phys. Rev. B **76**, 094407 (2007), and references cited therein.
[22] M. Buess, T. Haug, M. R. Scheinfein, and C. H. Back, Phys. Rev. Lett. **94**, 127205 (2005).
[23] G. Gubbiotti, G. Carlotti, T. Okuno, T. Shinjo, F. Nizzoli, and R. Zivieri, Phys. Rev. B **68**, 184409 (2003).
[24] J. K. Ha, R. Hertel, and J. Kirschner, Phys. Rev. B **67**, 224432 (2003).
[25] R. Zivieri, G. Santoro, and A. Franchini, J. Phys.: Condens. Matter **19**, 305012 (2007).
[26] G. N. Watson, *A Treatise on the Theory of Bessel Functions*, 1st ed. (Cambridge University Press, Cambridge, 1922), Chap. 13, p. 390.